

1 **Preprint of the following paper :**
2 Mancini, D. and Lane, S. N., 2020. Changes in sediment connectivity following
3 glacial debuttressing in an Alpine valley system. *Geomorphology*,
4 352, Article Number: 106987
5 Final published version available at
6 <https://www.sciencedirect.com/science/article/pii/S0169555X19304787>

7
8
9 **Changes in sediment connectivity following glacial debuttressing in an**
10 **Alpine valley system**

11
12 **D. Mancini^a & S.N. Lane^a.**

13
14 ^aUniversity of Lausanne, Institute of Earth Surface Dynamics, CH-1015 Lausanne, Switzerland

15
16 **Abstract**

17
18 Increasing air temperature and declining winter snowfalls are resulting in rapid glacier
19 recession and the expansion of proglacial margins in Alpine regions. Such margins include
20 substantial debris accumulations (e.g. frontal/lateral moraine ridges; till-covered and steep
21 valley sidewalls) which may be unstable due to glacial debuttressing. Rainfall, snowmelt and
22 ice melt out may then cause mass movements. Here, we quantify the decadal-scale erosion
23 and deposition patterns and changes in connectivity for two valley sidewall
24 geomorphological systems following retreat of the Glacier d'Otemma, Switzerland. We apply
25 archival digital photogrammetric methods to the period 1964 to 2009 to determine high
26 resolution digital elevation models. These were differenced to calculate patterns of erosion
27 and deposition and to quantify the evolution of sediment connectivity. We found that gully
28 headward erosion (rates between ca. -10.6 mm/yr and -1002.1 mm/year) was the main
29 geomorphological process during glacier thinning but increasing depositional rates
30 downslope of the gullies (ca. +21.3 to +298.5 mm/yr) were recorded in the following years
31 associated with significant alluvial fan growth at the slope base. Whilst gullying enhanced
32 connectivity by removing glacially conditioned sediment transfer buffers, so connecting side-
33 slopes to upstream sediment sinks (the upslope contributing area between 1964 and 2009
34 increased by +73.8% and +195.1% in each subsystem), alluvial fans reduced the rates of

35 sediment transfer to the rapidly enlarging glacial forefields. The detail of these responses is
36 conditioned by three generic processes: (1) the wider geomorphic setting – here, the
37 presence of a moraine bastion as a primary part of the sediment cascade strongly influenced
38 gully morphology evolution and the likely length of the paraglacial period length; (2) the
39 thickness of sediment left by the retreating glacier which controlled the influence of bedrock
40 topographic buffers on connectivity; and (3) the extent to which diffusive drainage systems
41 develop in response to the deposition at the hillslope base, which tends to disconnect
42 sediment flux. Post-glacially, gully development has a self-limiting effect on sediment
43 connectivity in that whilst gullying increases sediment connectivity, the eroded sediment
44 leads to deposition on the alluvial plain that reduces sediment connectivity.

45
46 **Keywords:** Climate warming; Glacial debuitressing; High mountain regions dynamics;
47 Paraglacial; Sediment connectivity; Historical evolution.

48
49 **Highlights:**

- 50
51
- 52 • Presents one of the first multi-decadal scale records concerning valley sidewalls
53 response, in term of geomorphological processes and connectivity, to rapid glacial
54 retreat and debuitressing.
 - 55 • Connectivity develops in response to glacial recession and thinning by gully
56 headward erosion.
 - 57 • Connectivity impacts morphodynamics, and vice-versa. Paraglacial
58 geomorphological features may extent the paraglacial period through secondary
59 reworking of sediment.
 - 60 • Gullying process increase the vertical connectivity (basin scale) but it may decrease
61 the lateral connection within the gully network (local scale).

61
62 **1. Introduction**

63
64 High mountain regions are strongly sensitive to climate change. The rapid recession of
65 Alpine glaciers and permafrost zones following recent atmospheric temperature rise is well
66 documented (Haeberli et al., 1997; Haeberli and Beniston, 1998; Fischer et al. 2014, 2015).
67 Since the end of the Little Ice Age (LIA), mean annual atmospheric temperatures (MAATs)
68 in the European Alps have increased by about +2°C, generating widespread negative glacier
69 mass balance and ice volume loss (Bauder et al., 2007; Fischer et al., 2015). European
70 Alpine glaciers lost c. 50% of their surface between 1850 and 2000 while Swiss glaciers,
71 based on the last Swiss glacier inventory of 2010, retreated by c. 40% (Paul et al., 2004;
72 Zemp et al., 2006; Fischer et al., 2014). The result has been a substantial increase in the
73 size of proglacial margins, by 920 km² in Switzerland and Austria since the end of the LIA
74 (Carrivick et al., 2018).

75 Proglacial margins are characterized by over-steepened slopes and unconsolidated
76 sediment accumulations, often unstable, and acting as potential sediment sources
77 (Ballantyne, 2002a,b; Laute and Beylich, 2014) notably during extreme events (Wulf et al.,
78 2012). The period of landscape reworking that follows is commonly referred to as
79 “paraglacial”, ending with a new and more stable deglaciated state (Church and Ryder,
80 1972; Cossart et al., 2008; Porter et al., 2010; Carrivick and Heckman, 2017). During the
81 paraglacial phase, an increase in the availability of glaciogenic deposits may accelerate the
82 down valley sediment cascade (Ballantyne, 2002a; Cossart and Fort, 2008) especially
83 because such deposits are commonly poorly sorted, including a relatively easily eroded fine
84 sediment fraction (Derose et al., 1998). The geomorphic consequences of glacier retreat are
85 well described in the scientific literature. On over-steepened rock slopes, glacier
86 debuitressing may result in major rockfalls and landslides as glacier retreat destabilizes
87 slopes through undercutting and, at the same time, the progressive loss of pressure exerted
88 by ice on slopes may result in rock stress-releases (Cossart et al., 2008; McColl, 2012; Davis

89 et al., 2013; McColl and Davis, 2013). Moraine accumulations may act as important
90 sediment sources after glacial retreat as shown for the European Alps (e.g. Curry et al.,
91 2006; Cossart and Fort, 2008; Carrivick et al., 2013; Lane et al., 2017), Western Norway
92 (e.g Ballantyne and Benn, 1994; Mercier et al., 2009; Laute and Beylich, 2012), and
93 Canadian Rocky Mountains (e.g Hugenholtz et al., 2008). It is thought that the glacier
94 advance that took place during the Little Ice Age slightly enhanced geomorphological activity
95 during the subsequent paraglacial phase (Laute and Beylich, 2013), in terms of headward
96 erosion of gullies and occurrence of debris flows, affecting debris covered slopes located
97 inside Little Ice Age margins (Laute and Beylich, 2012).

98 On moraine accumulations, buried ice melt, sediment mass failures and erosion by water,
99 including formation of debris flows, may encourage an erosional response (Evans and
100 Clague, 1994; Laute and Beylich, 2012, 2014) and the formation of complex gully systems
101 (Ballantyne and Benn, 1994; Lane et al., 2017). Hydrological processes may erode lateral
102 moraines at measured rates of 49 to 151 mm/year in the European Alps (Curry et al., 2006),
103 50 to 100 mm/year in Norwegian glacierized catchments (Ballantyne and Benn, 1994) and
104 0.4 and 31 mm/year in the Nepalese Himalaya (Watanabe et al., 1998). Gully development
105 acts as a source of sediment and encourages upstream to downstream connection of
106 sediment but also lead to debris fan and alluvial fan formation at the slope base (Lane et al.,
107 2017). Carrivick et al. (2013) reported alluvial fan growth in the Austrian Alps at a rate of 7
108 m³/day due to contemporary reworking of moraine-derived material formed during the Little
109 Ice Age. The diffusive nature of alluvial fans may reduce rates of sediment flux to the alluvial
110 plain where it can be reworked fluvially, representing an important potential negative
111 feedback towards the end of the paraglacial period (Church and Ryder, 1972; Mercier, 1997,
112 2008; Ballantyne, 2002a,b; Lane et al., 2017). Such changes may have wider impacts upon
113 proglacial sediment budgets (Carrivick et al., 2013; Staines et al., 2015).

114 This body of work suggests that evolving sediment connectivity may provide a conceptual
115 basis for explaining changing sediment flux during the paraglacial phase following rapid
116 glacier recession (Baewert and Morche, 2014; Heckmann et al., 2016). Such understanding
117 is crucial as the duration and intensity of the paraglacial phase will be partly a result of the
118 balance between connectivity increasing (i.e. positive feedbacks) and connectivity-reducing
119 (i.e. negative feedbacks) processes following glacier recession. The sensitivity of sediment
120 flux to connectivity in paraglacial environments is likely to be increased because glaciers
121 create landforms (e.g. lateral moraine ridges) which may interrupt the sediment cascade
122 (Brardinoni and Hassan, 2006; Cossart and Fort, 2008; Fryirs, 2013; Lane et al., 2017).
123 Such interruptions are unlikely to be permanent, as glacier retreat and thinning leads to base
124 level fall that can activate gullying and headward erosion (Schiefer and Gilbert, 2007;
125 Cossart and Fort, 2008) eventually dissecting such buffers (e.g. Gomez and Purdie, 2018;
126 Lane et al., 2017).

127 This paper builds on past studies of proglacial landscape evolution following glacier retreat
128 whether descriptive (e.g. Mercier, 1997; Ballantyne, 2002b), or more quantitative (e.g.
129 Warburton, 1990; Ballantyne and Benn, 1994; Schiefer and Gilbert, 2007). Research has
130 considered connectivity in deglaciating environments in general (e.g. Schrott et al., 2006;
131 Carrivick et al., 2013; Baewert and Morche, 2014; Carrivick and Heckmann, 2017), and
132 hydrological connectivity in particular (e.g. Cavalli et al., 2013; Lane et al., 2017). Here we
133 aim to provide one of the first quantitative assessments of how hillslope sediment
134 connectivity evolves at the decadal time-scale following from glacier thinning and retreat.
135 Such research is not straightforward because unlike glaciers themselves, the hillslopes that
136 form following their retreat are rarely monitored (Carrivick et al., 2015). Extracting
137 topographic information from archival imagery using photogrammetry is one solution to this
138 information and this has now been tested and applied for such zones over decadal time-
139 scales (e.g. Schiefer and Gilbert, 2007; Micheletti et al., 2015a, 2015b; Staines et al., 2015).

140 The development of the software used in Structure from Motion Multi-View Stereo (SfM-
141 MVS) photogrammetry (Westoby et al., 2012; Fonstad et al., 2013) opens up the potential
142 of this kind analysis to a wider community even if the way it is used has to be modified for
143 the large format imagery typical of archives (Bakker and Lane, 2017). The work is focused
144 on a Little Ice Age lateral moraine in the Otemma Valley, south-west Switzerland, in a
145 context of rapid climate warming and rapid glacier recession. It is representative of many
146 Alpine valley glacier systems where glacial erosion has created a relatively wide valley floor
147 combined with steep valley sides.

148

149 **2. Methodology**

150

151 2.1 Study site and climatic context

152

153 The proglacial margin of the Glacier d'Otemma is at an altitude of 2450 m a.s.l., just below
154 the lower limit of the discontinuous permafrost belt (Lambiel and Reynard, 2001; Deluigi et
155 al., 2017) (Figure 1). Mean Annual Air Temperature (MAAT) increased by +1.7°C during the
156 20th Century, but this increase was not uniformly distributed and there have been four main
157 phases; a relative stable and cold period until the 1940s; a rapid warming lasting for about
158 two decades; a cooler epoch between the 1960s and mid-1980s; and finally a warmer phase
159 which extends until today. Since the 1960s, the start of our study, the increase is c. +1.4°C
160 (Figure 2).

161 Even if this climatic trend is a common across the European Alps, evolution of the Glacier
162 d'Otemma is different to most other glaciers in the region. With some exceptions (e.g.
163 Gabbud et al., 2015), most Swiss Alpine valley glaciers saw a temporary re-advance in the
164 1970s and 1980s and then very rapid recession since (Haeberli and Beniston, 1998; Bauder
165 et al., 2007, Fischer et al., 2015). It is only the longer and less steep glaciers that tend to
166 show continual recession. The snout of the Otemma glacier retreated continually by 462 m
167 between 1900 and 1967 (6 m per year, Figure 2). There was a temporary acceleration in

168 retreat between 1967 and 1975 (to 42 m per year, Figure 2) suggesting some delay in glacier
169 recession in response to the warming that started in the 1940s and reflecting the long length
170 of the glacier (c. 9 km in 1964) and so the longer glacier response time. Recession of the
171 Otemma glacier slowed from 1975 until the early 1980s (to 11 m per year; Figure 2),
172 probably reflecting the relatively cooler period from the mid-1960s to the early 1980s. From
173 the early 1980s, glacier recession rates increased to c. 32 m per year until the early 2000s
174 and then to c. 50 m per year until present. The recession rate increases are probably
175 explained by the reduction of winter snow accumulation by c. -50% in the region between
176 the mid-1980s and 2010 (Micheletti et al., 2015b), coupled to higher MAATs. In summary,
177 the Glacier d'Otemma has retreated by 2110 m since the 1950s, losing about 60% of its
178 volume and 40% of its surface (Figure 2; GLAMOS, 2016; Lambiel and Talon, in press). In
179 addition, between 1964 and 2009, where the glacier has not the completely disappeared
180 from the study area, the glacier surface has lowered by c. -110 m (Figure 1b).

181 Today, the Otemma proglacial area is characterized by an alluvial plain reworked almost
182 continually by a braided river and unvegetated hillslopes and Little Ice Age lateral moraines,
183 about 200 m above the valley floor (Figure 1A). The moraines are, as is often the case in
184 Alpine deglaciating valleys, a consequence of glacier advance in periods within the Little Ice
185 Age (LIA) between 1350 and 1850. These moraines and the hillslopes beneath them have
186 become progressively de-buttressed following glacier recession. The study is focused on a
187 300 m length of the right lateral moraine exposed South-South East (Figures 1A-square a,
188 and 1B). Directly above the study area there is a moraine bastion, built up by the smaller
189 Glacier de la Grande Lire (Figure 1A-square c) which accumulates sediments resulting from
190 physical and chemical weathering, as well as the mechanical glacial erosion of granitic
191 bedrock (gneiss with highly-foliated minerals such as quartzite and mica). Grain sizes range
192 from sands to small boulders ($\varnothing < 2$ m). This moraine bastion is clearly the main supply to
193 the sediment cascade of the study area.

194 The moraine itself is partly discontinuous as there are some zones where moraine
195 accumulation did not occur and there are bedrock exposures. Directly above the LIA limit,
196 gravitational and torrential processes have reworked some sediments from the moraine
197 bastion generating several debris accumulations (Figure 1A-square b). The work has a
198 particular focus on two sediment sub-systems (Figure 1B). The first (SS1), located between
199 two massive rock outcrops in the most down-valley part of the study area, at elevations
200 between 2450 m a.s.l. and 2680 m a.s.l. (c. 41,700 m²), is characterized by a well-developed
201 torrential transport system connecting the moraine bastion to the alluvial cone (black dotted
202 line in Figure 1B). In 2017, when the work was conducted, it was situated c. 870 m from the
203 glacier terminus and it had a mean slope gradient of c. 62°. The second (SS2), situated c.
204 120 m up-valley from SS1, consists of a complex geomorphological system. It is located at
205 elevations ranging from 2460 m a.s.l. to 2720 m a.s.l. (c. 39,500 m²) and its sediment
206 cascade is initiated by sediment accumulation at the head of a gully system (gray dotted line
207 in Figure 1B). It is 750 m from the glacier terminus (based on the glacier's 2017 position)
208 with a mean slope gradient of c. 67°, slightly greater than SS1.

209 210 2.2 Methodological approach

211
212 Evolution of the moraine was studied both quantitatively and qualitatively using historical
213 aerial digital photogrammetry (Figure 3). Aerial imagery of the study area is available from
214 the 1960s. So, we decided to focus on the decadal timescale, following Micheletti et al.,
215 (2015a) and Staines et al. (2015). To determine the geomorphic evolution of the hillslopes,
216 archival digital photogrammetry was applied to historical aerial images to produce Digital
217 Elevation Models (DEMs) for seven years (T_x). The associated DEMs can be affected by
218 random and systematic errors, related to image quality, ground control point survey quality,
219 surface composition, topographic complexity and interpolation methods (Lane et al., 1994;
220 Lane, 1998; Hancock, 2006; Heritage et al., 2009), and this requires error management

221 which is explained below. Once the DEMs were corrected, they were used for two different
222 purposes. First, DEMs of Difference (DoDs) were used to quantify the patterns of erosion
223 and deposition for different periods. Second, assuming hydrological control as an important
224 factor in sediment reworking, we conducted a hydrologically-based sediment connectivity
225 analysis (after Lane et al., 2017). The Lane et al. (2017) approach differs from the approach
226 of Cavalli et al. (2013), because it seeks to make a distinction between DEM sinks that are
227 likely to be due to noise in the DEMs and those that are likely to be real, a product of the
228 structural organization of the landscape. These analyses were combined with detailed
229 geomorphological information, conducted through geomorphological mapping and analysis
230 of elevation profiles, with the aim of determining the evolution of the sediment cascade
231 through time. All data generated in this project are available at ebibalpin.unil.ch.

232

233 2.3 Methods

234

235 2.3.1 Archival digital aerial photogrammetry

236

237 Photogrammetry is a long-established remote sensing technique that has now been proven
238 for the reconstruction of long-term geomorphic changes in Alpine environments all over the
239 world, including river-floodplain systems (e.g. Lane et al., 2010; Watanabe and Kawahara,
240 2016; Bakker and Lane, 2017), glaciers (e.g. Immerzeel et al., 2014; Gabbud et al., 2016;
241 Mölg and Bolch, 2017), proglacial areas (e.g. Staines et al., 2005; Schiefer and Gilbert,
242 2007; Carrivick and Rushmer, 2009) and periglacial zones (e.g. Kääb and Vollmer, 2000;
243 Micheletti et al., 2015a). The principles of applying photogrammetry to historical archival
244 imagery are outlined in Lane et al. (1993). During the 1990s and 2000s, such approaches
245 were developed to make use of digital datasets which meant that access to expensive
246 hardware removed one of the major limits to the application of archival photogrammetry
247 (Micheletti et al., 2015a). These limits have been further reduced by the development of
248 SfM-MVS software which is both cheaper and faster than traditional digital photogrammetry

249 software. However, applying SfM-MVS software to archival imagery requires a very different
250 workflow to that associated with conventional SfM-MVS applications (e.g. Westoby et al.,
251 2012; Fonstad et al., 2013) which use specially-acquired imagery. Bakker and Lane (2017)
252 showed that because the number of images, and hence the extent of image overlap in
253 archival datasets, is substantially lower than is normal with specially-acquired imagery, SfM-
254 MVS software struggles to reconstruct the correct interior geometry of the cameras used for
255 data acquisition. As a result, we followed more classical archival methods but applied them
256 using SfM-MVS software.

257 The historical images used in this work were provided by the Swiss Federal Office of
258 Topography (SwissTopo) for seven distinct dates between 1964 and 2009 (Table 1).
259 Camera certificates were available for each period and, rather than determining them using
260 the SfM-MVS software, we followed Bakker and Lane (2017), and fixed the calibrated focal
261 lengths, and tangential and radial lens distortions as proscribed in the camera calibration
262 certificates. The SfM-MVS software was then used to reconstruct the position and
263 orientation of the cameras at the time of acquisition (Figure 4).

264 We use the commercial software Pix4D[®] for the photogrammetric analyses. The camera
265 calibration certificate was used to specify the calibrated focal length and the tangential and
266 radial lens distortion for each image. Working in the Swiss CH1903 coordinate system, we
267 manually inserted the initial coordinates of the principal point position of every uploaded
268 image provided by SwissTopo. To aid the initial solution of the collinearity equations, we
269 included Ground Control Points (GCPs) (Fonstad et al., 2013). GCP collection followed
270 Micheletti et al. (2015b). A Trimble[®] R10 dGPS was used establishing the base station on a
271 fixed point and left recording at 1 minute intervals for 12 hours (Figure 5). These coordinates
272 were then corrected *post hoc* using the continuously recording dGPS network SwissPos[®],
273 with data taken from the Lausanne and Zermatt stations. The base station precision was
274 better than ± 0.01 m in the horizontal and ± 0.02 m in the vertical after correction. The stable

275 points, commonly very large boulders and bedrock outcrops, were measured in a real-time
276 kinematic survey, with data point precision of ± 0.01 m in the horizontal and ± 0.02 m in the
277 vertical. These were also corrected *post hoc* to the SwissPos-corrected base station. The
278 choice of GCP locations had the initial goals of: (i) a good distribution across the study area
279 (Küng et al., 2011; Javernick et al., 2014) and (ii) long-term stability and accessibility
280 (Micheletti et al., 2015b). The latter was the principal requirement; this meant in practice that
281 we had to relax the former, but noting that with the SfM-MVS photogrammetric software, the
282 bundle adjustment uses conjugate features identified from across the area of interest, so
283 increasing the robustness of estimations in zones beyond where the GCPs were measured.
284 In total, we were able to measure 13 stable GCPs. Due to the stability criterion, they are
285 concentrated in the southern part of the LIA proglacial margin (Figure 5).

286 An initial block bundle adjustment solution was obtained using 3 GCPs. Then, additional
287 GCPs were added manually to improve the solution, minimizing the Root Mean Square Error
288 (RMSE), and a point cloud was generated. The bundle adjustment used between 4 and 8
289 GCPs (Table 2), which is a relatively small number compared to the total surface covered
290 by the aerial images (c. 29,000 m²), and a total number of tie-points per image between
291 36,341 and 93,388 points. If the bundle adjustment has been a success, the theoretical
292 precision should be commensurate with or better than the mean RMSE, which it is for 1970
293 1977, 1983 and 2009. It is slightly degraded for 1964 and 1995 and more so for 1988. Some
294 degradation was expected for 1964, as the number of tie-points used is relatively low, related
295 to the poorer scan resolution (Table 2), which reduced image texture and also resulted in
296 poorer DEM resolution and higher georeferencing error. The horizontal errors are generally
297 low, but this is less the case for 1988, which explains the higher RMSE. It is likely that there
298 is some error in precise positioning of GCPs during digitization which may also explain the
299 higher σ_z (Table 2). Generally, higher resolution imagery with a better theoretical precision,

300 produces lower σ_z , the exception being 1988 with degraded σ_z and 2009 with better than
301 expected σ_z .

302

303 Even with acceptable RMSE values, with SfM-MVS software it is possible that the DEMs
304 contain residual systematic error, such as tilt or doming (Bakker and Lane, 2017). Lane et
305 al. (2004) showed that although this error is systematic, it commonly results from residual
306 random uncertainty associated with parameters in the collinearity equations. Commonly, it
307 is only notable when consecutive DEMs are compared (Lane et al., 2004). As a result, we
308 randomly sampled 98 points from stable zones, the latter restricted to bedrock outcrops
309 (Figure 6) and so should have constant z values. We considered the three dates that had
310 the most GCPs and on this basis noted that 1983 had the best RMSE. Thus, 1983 was taken
311 as the baseline. We then took the planform position of each of the 98 points and estimated
312 the corresponding z values in the derived DEMs using the respective final bundle adjustment
313 for each DEM. We compared all z elevations to the 1983 DEM z elevations. Table 3 (before
314 correction) reveals that the mean error was high suggesting the presence of systematic error
315 which would also inflate the standard deviations of error. This pointed to the need to remove
316 systematic error before the DEMs could be used to calculate DEMs of difference and
317 confirms the findings of Bakker and Lane (2007) in a similar archival application using SfM-
318 MVS software.

319

320 2.3.2 Post-processing of point clouds

321

322 Systematic errors were removed by co-registration onto a single reference point cloud using
323 CloudCompare[®] (Miller et al. 2008; Micheletti et al., 2015c; Bakker and Lane, 2017). To
324 better manage the registration, we limited the point clouds to our study area with a total
325 coverage of ca. 0.20 km² (Figure 1B). Visually, and also taking the arguments above, the
326 best point cloud appeared to be that of 1983 and all point clouds were co-registered onto

327 this one. We identified features that had to be stable during the study period (primarily
328 bedrock outcrops but also large boulders) and used it in the iterative adjustment method in
329 CloudCompare to minimize the RMSE between each point cloud and that for 1983 (table 4).
330 Final RMSEs values were comprised between 1 and 0.1 with a decreasing order from the
331 oldest point cloud to the most recent (Table 4). Note that, even if the point cloud of 1964 had
332 a higher point cloud density compared to others, notably 1988 and 1995, the resulting RMSE
333 is the highest; it reflects the poor imagery resolution at the lower altitudes that did not allowed
334 clear definition of geomorphic features.

335 After co-registration, 1 m resolution DEM grids were created in Arcmap 10 using kriging.
336 This interpolator is recognized to be the best solution for complex landscape surface data
337 because of its ability to conserve larger-scale topographic detail (Moore et al., 1991; Holmes
338 et al., 2000). We chose to use an ordinary spherical semi-variogram leaving the software to
339 find the best values for the fitting parameters (sill and nugget).

340 Finally, to reduce linear systematic DEM error further, we adopted a multi-regression method
341 using stable zone elevation values in order to better fit individual DEMs to the reference. In
342 practice, we compared observed elevations (Z^0) with those predicted by the mathematical
343 model (Z^p) and, in order to increase their correlation coefficient (r) until a minimum reference
344 value of 0.9, we iteratively deleted outlier values. Once calibrated the regression model has
345 been applied to every cell composing the DEM (Table 5). The combination of point cloud
346 registration and tilt removal resulted in a substantial decrease in systematic error and
347 precision (Table 3)

348 Resulting DEMs were used to detect both historical surface geomorphological changes, to
349 relate these to a geomorphological map of the area (Lambiel et al., 2016), and to quantify
350 changes in hydrologically-driven sediment connectivity through time. Our focus is upon
351 evolution within the Little Ice Age limit which we base upon a marked difference in vegetation

352 development as well as the distribution of moraine ridges. Due to slope pressure releases
353 triggered by deglaciation, and consequent mass movements, it is possible that ice surface
354 altitude at the LIA maximum has been underestimated (Cossart et al., 2008). In the text,
355 when we refer to the LIA limit, we assume that this is not the case.

356

357 2.3.3 Calculation of DEMs of difference

358

359 DEMs of difference (DoD) were calculated to determine erosion and deposition patterns
360 (Lane et al., 2003). This latter is based on a simple matrix subtraction ($T_{X2}-T_{X1}$) between
361 DEMs (Brasington et al., 2003; Lane et al., 2003). In practice, we then needed to account
362 for residual uncertainties in the dataset (Brasington et al., 2003; Lane et al., 2003), related
363 to (i) the quality of individual points in point clouds, (ii) the density of points available to
364 represent the surface, (iii) the distribution of points within the study area and (iv) the
365 interpolation method used to generate regular surface within points (Lane et al., 1994; Lane,
366 1998; Hancock, 2006; Heritage et al., 2009). In our case, we generated very high point
367 densities, with very few zones of interest not covered, and so the primary focus was upon
368 the uncertainty due to the quality of individual points. Thus, we used a simple error
369 propagation method (after Lane et al., 2003) to investigate the propagation of error in
370 individual DEMs of difference, which was defined as the level of detection needed for an
371 elevation change to be judged as significant. After Lane et al. (2003) this was defined as:

372

$$\text{LoD} = \pm t \sqrt{(\sigma_{DEM1})^2 + (\sigma_{DEM2})^2} \quad (1)$$

373

374

375

where: LoD = Limit of Detection threshold

376

t = Student's confidence interval threshold value (1.96 at 95% or 1 at 68%)

377

σ_{DEM1} = standard deviation of DEM₁ Z error

378

σ_{DEM2} = standard deviation of DEM₂ Z error

379

380 The standard deviation of individual DEM errors was calculated from a sample of 98
381 manually identified Z values representing spatially distributed stable zones recognizable on
382 all georeferenced DEMs (Figure 6). We took a confidence interval for t of 68% as higher

383 confidence intervals tend to overlook smaller magnitude but spatially homogeneous
384 changes (Wheaton et al., 2010) and because this threshold produced visually plausible
385 patterns of erosion and deposition. The resulting LoD values (Table 6) were used to
386 threshold the historical DoDs in order to show only statistically significant geomorphological
387 changes; values within the LoDs are classified as no significant change between dates.

388 389 2.3.4 Hydrological sediment connectivity analysis

390
391 Sediment connectivity is defined as the degree to which sediments can flux through the
392 landscape, and in particular between sediment sources and downstream areas (Cavalli et
393 al., 2013). The focus in this manuscript is on hydrological sediment connectivity, that is the
394 water-driven transfer of sediment between two different compartments of a catchment
395 sediment cascade (Fryirs, 2013). We assume that a sediment disconnection follows from
396 when a sediment sink forms and removes sediment from the cascade for varying lengths of
397 time (Fryirs, 2013; Bracken et al., 2015). In our study, the connectivity analysis has two main
398 related objectives. The first is to detect the evolution of sediment sources and sinks on
399 hillslopes within the LIA limits, as well the water-related sediment transport paths, starting
400 from the analysis of DoDs and orthoimages. DoDs are used to investigate the functional
401 connectivity of the system (i.e. sediment transfer between compartments) and, through their
402 comparison with orthoimages, quantify the main sediment pathways and their evolution
403 through time. The second is more focused on the analysis of the structural (dis-)connectivity.
404 Following Lane et al. (2017), it investigates the distinction between natural and artificial
405 sediment disconnections and their evolution through time. Sediment disconnection may be
406 confused with DEM-related noise (Borselli et al., 2008; Cavalli et al., 2013; Lane et al., 2017),
407 especially in DEMs derived from archival imagery with reduced precision as compared with
408 specially-collected imagery. Here, we define natural disconnection as the flow path
409 obstruction by a geomorphological feature that leads to a reverse slope (e.g. due to glacial

410 or paraglacial landforms), while artificial disconnection is that caused by DEM noise. The
 411 identification of sediment flow paths starting from DEM data is commonly undertaken by
 412 forcing flow accumulation through filling all depressions regardless of their nature, and which
 413 risks removing disconnection that is natural rather than artificial (Arnold, 2010). As we are
 414 interested in determining the impact of the evolution of the moraine morphology on sediment
 415 connectivity between 1964 and 2009, we applied the methodological approach proposed by
 416 Lane et al. (2017) which captures how the level of hydrological connectivity evolves as a
 417 DEM is progressively filled. If there is a transition from small to large upslope contributing
 418 areas at fills below or close to the DEM noise, it is likely that a flow path is hydrologically
 419 connected. Where the transition occurs at higher magnitudes of fill, so it becomes more
 420 likely that the disconnection is real, the greater the level of fill, the greater the probability.
 421 Our approach uses the TopoToolbox (Schwanghart and Kuhn, 2010) to apply the Holmgren
 422 (1994) flow routing to calculate the upslope contributing areas (A : defined as the area
 423 upslope of a surface element that drains to that element; Rieger, 1998) with different levels
 424 of DEM fill. The Holmgren routing uses:

$$425 \quad FD_{(j)} = \frac{(tanB_j)^x}{\sum_{j=1}^n (tanB_j)^x} \quad (2)$$

426 where: $FD_{(j)}$ = proportion of hydrological flow in direction j
 427 B_j = slope gradient between the central cell and the cell in direction j ; with B_j set to zero if B_j is negative in the
 428 downslope direction
 429 n = number of slopes positive in the downslope direction
 430 x = variable exponent varying between 0 and infinity
 431
 432

433 Equation 2 determines for each DEM cell the proportion of flow going in a specific direction.
 434 For $x=0$ flow is equally distributed in all directions regardless of slope; for $x=1$ flow is
 435 proportionally divided to all downhill cells as a function of slope gradient (multi-directional
 436 flow) and for $x = \infty$ all runoff is directed along the line of steepest descent (i.e. D8 algorithm)
 437 (Quinn et al., 1991; Holmgren, 1994; Lane et al., 2017). In our study, we decided to use
 438 variable x values ($x=1,2,4,8,16$ and 32) to determine their effects. The fill value begins at 0.1

439 m and is then increased dyadically to a maximum of 102.4 m (i.e. we double the fill level
440 starting from 0.1 m and ending with 102.4 m). In the case of artificial disconnection (dotted
441 line in Figure 7), we would expect a rapid increase in A when the level of fill (K) reaches
442 values comparable to DEM noise (σ_{2009}). However, in the presence of natural disconnection
443 (solid line in Figure 7), the A increase may be later ($K > \text{DEM precision}$) and also achieved in
444 a number of steps if there a number of natural disconnections of different magnitude. To
445 apply the method, accumulation is determined for identified cross-sections on the hillslope.
446 By comparing curves, it is possible to determine how connection evolves through time. If, at
447 the most recent date, perfect connection (i.e. a rapid increase in A to A_1) is reached at lower
448 levels of K , it implies that hydrological connection has improved upstream through, for
449 example, gullying (“within-basin connection” dotted line Figure 8). If, at the same time, the
450 asymptote is reached at a higher value of A , i.e. A_2 , then it means that the geomorphic
451 processes have been sufficient to improve connections upstream of the area associated
452 with A_1 (“basin extension”; dash-dotted line Figure 8). It is also possible that blockages along
453 a flow path develop as a result of erosion or that geomorphic processes elsewhere capture
454 some of the upslope contributing area of the basin, causing the value of A linked to the
455 asymptote to decline. Likewise, the establishment of a new natural disconnection, for
456 example the interruption of gully channels though a landslide dam, could cause the curve to
457 shift towards a higher level of fill.

458 In these analyses, our focus is on two sets of data. The DEMs for 1964 and 2009 extended
459 right up to the basin divides above the two focus study areas. For these we visualize the
460 connectivity and quantify how it is changing with the connectivity analysis. For the other
461 dates, only part of the possible upstream contributing areas was in the DEMs and so we do
462 not include these, except for visualization. We make one exception to the latter. We quantify
463 the distribution of upslope areas for all cells within each system. To make these comparable

464 between dates, we delimit the cells using a mask defined by the smallest DEM extent in the
465 time series, such that the areas being compared between dates are the same.

466 467 **3. Results**

468 469 3.1 Geomorphic change between 1964 and 2009

470
471 The visual evolution of the lateral moraine is showed in Figures 9 for 1964, the beginning of
472 the study, and in Figure 11 for 2009, the end of the study. Figure 10 compares the elevation
473 profiles of the subsystems. The LIA limit is shown as a discontinuous moraine ridge (Figure
474 9B). Above it, the hillslope is almost totally covered by a stable soil-vegetation complex,
475 indicating relatively low levels of geomorphic activity, except for the Glacier de la Grande
476 Lire's moraine bastion and its depositional zone immediately below. This zone is comprised
477 of non-cohesive sediments, fines to small boulders ($\varnothing < 2$ m), and it appears to be dynamic
478 given the absence of vegetation (I in Figure 9A).

479 The spatial configuration of the hillslope in 1964 is an important aspect to consider because
480 it allows the identification of potential sediment transport paths and buffers. The remains of
481 the moraine crest, mainly visible on the rock outcrops, are likely to represent barriers for
482 sediment connectivity in both subsystems (Figure 9B). Nevertheless, the geomorphological
483 map (Figure 9B), the elevation profiles (Figure 9C and Figure 10) and the flow accumulation
484 algorithm (Figure 9E) show that other potential obstructions to downward sediment transport
485 are likely to be present. In SS1, we identified three more buffers (II to IV on Figures 9B, 9C
486 and 10): the flatter zones located on the moraine bastion (II), the flatter area behind the LIA
487 limit (III) and the concave fluvial scar just above the gully system (IV). In contrast, SS2 has
488 a more complex profile resulting in the presence of more potential buffers (V to VIII on
489 Figures 9B, 9C and 10) identified in: the flatter regions on the moraine bastion (V), the fluvial
490 scar with multiple terraces behind the LIA limit (VI), the accumulation at the head of the
491 gullies (VII) and the top of the supraglacial alluvial fan that would have formed on the glacier

492 before its retreat (VIII). In general, all the above-mentioned obstacles are flatter zones
493 constructed by the interaction between the bedrock outcrops and the reworked moraine
494 sediment composing the debris-mantled slope during the LIA and post-LIA periods.

495 The situation in 2009 shows landscape evolution after glacier retreat and debuttressing
496 (Figure 11). The most important geomorphological change concerns the growth of massive
497 alluvial fans at the intersection between the hillslope and the alluvial plain once occupied by
498 the Glacier d'Otemma (IX on Figure 11B). These fans may be related to greater upslope
499 coupling, following from gully headward erosion activated in response to the glacier thinning,
500 which progressively eroded the debris-mantled slope and accumulations previously
501 identified as potential buffers (Figures 10 and 11C). This process led to the development of
502 a torrential stream system able to couple even more distant sediment sources (Figure 11E).
503 However, subsystems were affected by different intensities of gullying. In SS1 gullies
504 developed upslope reaching the moraine bastion, while in SS2 they eroded without any
505 important upward extension (Figure 11B).

506 Figure 12 quantifies these changes in terms of DEMs of difference for SS1 between 1964
507 and 2009. During the phase of glacier recession between 1960 and the mid-1970s, there is
508 substantial glacier loss and thinning, of about 50 m (figure 1B), and hence debuttressing.
509 This is likely to have resulted in both gully incision and headward erosion (I on Figures 12A
510 and 12B). If this delivered more sediment to the alluvial fans below, it would explain their
511 increasing basal area and total volume (II on Figures 12A and 12B). At the end of the 1970s,
512 the glacier completely disappeared leading to exposure of the valley bottom (III on Figure
513 12C). But, the stabilization of the hydrological base level does not interrupt the geomorphic
514 response to glacial debuttressing. Since the 1980s, there has been a more intense erosion
515 reworking of c. -2 and -7 m of moraine material per decade, and the gully head extends into
516 the moraine bastion and there was the removal of the intermediate sediment sink behind the
517 LIA ridge (I on Figures 12D, 12E and 12F). At the same time, the alluvial fan experienced

518 continuous aggradation (c. +2 and +7 m per decade; II on Figure 12D, 12E and 12F) only
519 interrupted during the 1983-1988 period, when we recorded surface lowering rates between
520 c. -2 and -9 m (IV on Figure 12D). Pioneer vegetation developed on the glacio-fluvial plain
521 but not on the gully-alluvial fan system indicating that sediment reworking from the moraine
522 bastion is still today relatively active.

523 Figure 13 shows the historical geomorphological evolution of SS2. In this case, the fluvial
524 processes occurring in response to the glacial debuitressing are mainly located below the
525 LIA limit, only partially affecting the flatter zone located above the gully system. During
526 deglaciation, which for this part of the hillslope lasted until the end of the 1980s, Figure 13
527 suggests an initially weak fluvial activity (I on Figure 13A) followed by increased activity and
528 alluvial fan erosion (I and II in Figure 13B and Figure 13C). This latter is concurrent with
529 significant glacier thinning of c. 60 m, which occurred between the 1970s and the beginning
530 of the 1980s (figure 1B). Note that until the exposure of the valley floor, even in this case,
531 the alluvial fan shows erosional patterns because its aggradation rate was lower than the
532 glacial thinning. From the mid-1980s, similar to SS1, base level fell to the valley floor altitude
533 (III on Figure 13D) and headward gully erosion continued, with c. 2 to 6 m of reworked
534 sediments deposited on the alluvial fan (I and II on Figure 13D, Figure 13E and Figure 13F).
535 During the 1983-1988 period, up-valley, where the glacier thinning exposed a massive
536 bedrock patch at the interaction with the alluvial plain (IV on Figure 13D), fluvially-driven
537 erosion appeared to be less intense. The alluvial cone began to subdivide into two distinct
538 fans. In the 1988-2009 period further fluvial erosion, encouraged by the complete
539 disappearance of the glacier (III on Figure 13E), allowed sediment remobilization. Gully
540 incision (I on Figures 13E and 13F) took place with two different spatial intensities: on the
541 upslope section fluvial erosion reworked c. 6 m of moraine material exposing the underlying
542 bedrock (IV on Figure 13E), while on the downslope section, even if recorded rates are
543 higher (c. -15 m), complete denudation did not take place. The was major alluvial fan

544 aggradation, as with SS1, but also some basal erosion (II on Figure 13E and V on Figure
545 13F) and this may have reactivated headward gully erosion (c. 10 m) in the most downslope
546 area, where the moraine layer is still thick (I on Figure 13F). The reworked sediments
547 deposited (c. +6 m) immediately at the alluvial fan top prevented bedrock exposure (VI on
548 Figure 13F). Vegetative colonization took place on the alluvial scar, on the bedrock outcrops
549 and on the alluvial plain without affecting the gully channels and related alluvial fan.

550 If we combine these patterns together, the total volume of remobilized sediments in the two
551 studied systems was 1.8 km³, with 1.1 km³ related to SS2 and 0.68 km³ to SS1. If we
552 standardize these by their surface extents, both subsystem experienced intense erosion
553 rates until 1988, between -10 mm/year and -716 mm/year for SS1; and -31 mm/year and -
554 1002 mm/year for SS2. This period was followed by increased deposition with rates ranging
555 from 21 to 298 mm/year for SS1 and 21 to 170 mm/year for SS2. In general, there is a clear
556 trend towards decreasing sediment reworking rates over time (Figure 14).

557 558 3.2 Hydrologically-defined sediment connectivity

559 Given the geomorphic evolution described above, this section seeks to quantify the evolution
560 of hydrological connectivity. Figure 15 shows the upslope contributing area for both the 1964
561 and the 2009 DEM calculated with all pits filled using a fill threshold defined by the σ_{2009}
562 (Table 3). Figure 15 confirms that in 1964 there were drainage patterns present that can
563 also be found in 2009, such as below the moraine bastion associated with the Glacier de la
564 Grande Lire. The LIA moraine of the Glacier d'Otemma is not-well defined and continuous
565 in 1964, such that there is no clear glacially inherited obstacle to hydrological connection. If
566 there was one, it had been breached before 1960. In 2009, after complete glacial
567 debuitressing, the efficiency of the hydrological sediment connectivity has generally
568 increased as the hillslope is characterized by higher upslope contributing area values
569 (Figures 15 and 16).

570 Distributions of upslope contributing area (Figure 16) confirm the visual assessment above.
571 In SS1, cells having values between c. 0 and 10 m² (26.6% in 1964 and 18.5% in 2009) are
572 clearly diminished over time in favor of cells with higher values, especially ranging from 10⁴
573 to 10⁶ m² which increased from 31.3% in 1964 to 37.8% in 2009). Mean cell values increased
574 from 2750 m² in 1964 to 4790 m² in 2009 (+73.8 %). Histograms characterizing SS2 suggest
575 trends similar to SS1 but with different intensities. Cells showing cell values of c. 0 and 10
576 m² (27% in 1964 and 18.8% in 2009) diminished markedly, while pixels values comprised
577 between ca. 10⁴ and 10⁷ m² increased (38.9% in 1964 to 48.6% cells in 2009). In this
578 subsystem, the mean cell values in 1964 was 2820 m² compared to 8320 m² in 2009 (+195
579 %). In general, cells moved towards an overall higher upslope contributing area value.

580 Figure 17, shows changes in connectivity between 1964 and 2009 and highlights that the
581 increases in upslope contributing area appear to be related to the development of the gully
582 network, encouraged by headward erosion in response to gradual glacier thinning (Figure
583 10), connecting previously-separated geomorphological compartments and eroding features
584 once acting as barriers. In fact, the increase in connectivity is clearest along the gullies and
585 on the alluvial plain. Results suggest that between 1964 and 2009, at the hillslope scale,
586 headward erosion by gullies increased the total area of potential remobilizable sediments
587 by c. 24,810 m² (c. +3%, Figure 17). Given this, in 2009, regions with small accumulation
588 areas and disconnections, especially in regions located below the LIA limit, seem to be still
589 significant (Figure 15). As a result of better connectivity, it is possible that increased flux of
590 down-wasted sediments developed the alluvial fans at the hillslope base. Indeed, below the
591 1964 ice contact line, there is a tendency for flow to become more diffuse (Figure 15 and
592 17) suggesting a reduction in connectivity from this fan development.

593 Figure 16 also suggests that the evolution of connectivity was progressive and in some
594 cases could be discontinuous with increases in disconnection following increases in
595 connection. Histograms of upslope contributing area show that the total number of cells

596 having small values, attributable to a less efficient connectivity, experience a strong increase
597 during the 1977-1995 period. For SS1 there is an increase of the number of cells (+16%,
598 equivalent in area to 1252.6 m²) with values comprised between 10² and 10³. On the other
599 hand, this increase (9.4% equivalent to 1919.7 m²) concerned cells having values between
600 100 and 1x10⁴ m². Figure 18 clearly shows this phenomenon highlighting that at the same
601 time as the activation of new sediment sources through gullying, others regions, essentially
602 located near the main channel have become less connected (Figure 18D, 18E and 18F).
603 The connectivity clearly improved in 2009 when upslope contributing area values again
604 evolved towards higher values (Figures 16 and 18G).

605 The evolution of connectivity between 1964 and 2009 is quantified in Figure 16 in terms of
606 the relationship between the degree of pit filling and the upslope contributing area for
607 different values of the Holmgren routing parameters (Equation 2). In 1964, the sediment
608 connectivity in our study area was characterized by a general disconnectivity both above
609 and below the LIA limit. Figure 19 shows that all sampled locations have one or more abrupt
610 increases in basin contributing area reflecting the potential barriers (or sinks) identified in
611 Figures 9, 10 and 15. Geomorphological analysis and the upslope contributing area map in
612 1964 showed that these locations were characterized by both complex topography (such as
613 reverse slopes) and abrupt decreases in accumulated area immediately downstream . Given
614 this, is it also important to note that all transitions are at levels of fill greater than the DEM
615 related noise suggested by the σ_{2009} (Table 4), demonstrating the probable presence of
616 natural rather than artificial disconnections.

617 The quantification of the buffers affecting the hydrological sediment connectivity of SS1 in
618 1964 (samples I-III on Figure 19) did not suggest significant sinks. At the LIA limit region (I
619 on Figure 19) and on the moraine bastion (II in Figure 19), accumulated areas are c. 5.6 x
620 10⁵ and 9.3 x 10⁴ m² respectively and perfect connection is achieved through fills of 0.8 m
621 and 6.4 m, respectively. In contrast, the hydrological connectivity on the alluvial fan (III in

622 Figure 19) is characterized by two increases at 3.2 m and 12.8 m starting from an
623 accumulated area value of $7.3 \times 10^4 \text{ m}^2$, suggesting the presence of more complex
624 topography. In 2009, the hydrological sediment connectivity has increased as the fill levels
625 necessary to overcome obstacles are no longer present. Values for the accumulated area
626 remained stable at the LIA limit, suggesting that perfect connection was reached in 1964,
627 while it slightly increased for the moraine bastion ($7 \times 10^3 \text{ m}^2$) and the alluvial fan (2.7×10^4
628 m^2) (Table 7).

629 On the other hand, the SS2 data in 1964 (IV-IX on Figure 19) are all characterized by two
630 or more increases in upslope contributing area, between 3.2-6.4 m and 12.8-25.6 m of fill,
631 except for the moraine bastion summit (VIII on Figure 19) which has an additional small
632 increase at 0.8 m. This fact highlights that, at the beginning of the study, numerous buffers
633 affected the fluvial system making SS2 more disconnected than SS1. Concerning the
634 Holmgren parameter, in general we find a more concentrated flow on the moraine bastion
635 compared to the lower LIA section. The subsystem in 1964 was characterized by a wide
636 range of accumulated area comprise between $1 \times 10^2 \text{ m}^2$ for the moraine bastion ridge and
637 $6.3 \times 10^5 \text{ m}^2$ for its central part (Figure 19 and Table 7). In 2009, the efficiency of connectivity
638 increased and most of the sampled locations suggest the removal of barriers (IV, VI, VIII, IX
639 on Figure 19) or a reduction in their importance (V and VII on Figure 19). In these latter
640 cases, buffers are described by a fill level of 6.4 m and their continued existence is probably
641 due to, respectively, bedrock exposure and the crest of the moraine bastion. Nevertheless,
642 despite the limited extension of the gully shown on Figure 13, gully erosion may have been
643 important, especially on the lower LIA section, while on the moraine bastion it is the upslope
644 basin reorganization which drove the improvement of connectivity. The combination of these
645 mechanisms allowed major changes in the spatial configuration of the geomorphic
646 subsystem and the transition to a more diffuse flow. However, note that in the LIA limit
647 region, flow is concentrated and it may be related to recent headward erosion that affects

648 the flatter accumulation at the gully head (I on Figure 13F). In contrast, the markedly diffusive
649 flow characterizing the alluvial fan (IX on Figure 19) confirms how its formation is likely to
650 have reduce the connectivity between the slope and the proglacial margin. Changes in
651 accumulated area supports the above observation. In summary, in all zones where gullying
652 dominated (V, VI and VII in Figure 15), except for the LIA region were the situation remained
653 stationary, there was an increase in accumulated area; whilst in zones of deposition (VIII
654 and IX in Figure 15) reductions were noted (Table 7).

655

656 **4. Discussion**

657 4.1 Glacier dynamics and the geomorphic response of the lateral moraine

658 The Glacier d'Otemma has been in continuous retreat since the Little Ice Age (Figure 1 and
659 2), leading to the progressive debuitressing of its lateral moraines. Debuitressing involves
660 both glacier retreat and progressive thinning of ice, changes that lead to a local hydrological
661 base level fall and which may trigger paraglacial stress release and mass movement
662 (Cossart and Fort, 2008; Porter et al., 2010). As the glacier terminus moves up valley, there
663 was a tendency for up slope gully erosion of between -10 mm/year and -1002 mm/year and
664 deposition of reworked sediments with rates of ca. +21 mm/year and +298 mm/year on the
665 glacier surface, or valley bottom, in the form of alluvial fans. In some cases, especially in
666 SS2, erosion to bedrock was observed (Figure 13E). Fluvial incision rates are greater than
667 measurements of gully erosion on recently deglaciated terrains in Norway (30 mm/year and
668 170 mm/year; Ballantyne and Benn, 1994; Curry 1999) and the Swiss Alps (49 mm/year and
669 151 mm/year; Curry et al., 2006). Higher recorded rates in our study area may be related to
670 a difference geomorphological context, especially the presence of a moraine bastion or a
671 thicker till layer covering the slope left by the glacier, compared to previous works. It may
672 also reflect the exceptionally high rates of glacier recession. In contrast, measured rates of
673
674

675 alluvial fan aggradation fall within limits for Norwegian sites (8 mm/year and 44 mm/year;
676 Ballantyne, 1995) and with measurements recorded in Patagonian sites (330 mm/year and
677 400 mm/year; Harrison and Winchester, 1997). With glacier recession, and associated ice
678 surface thinning, the local base level falls, providing some temporary sediment storage for
679 the sediment cascade along the valley flank (Cossart and Fort, 2008). After deglaciation,
680 fans regulate the hydrological base level of the lateral moraine, but the response of the
681 sidewall continued also once the glacier terminus had moved further upstream (Figures 12D,
682 12E, 12F and 13F). Erosion of alluvial fan toes was ultimately controlled by fluvial activity in
683 the alluvial plain as observed more generally (Harvey, 1977, 1996; Lisenby and Fryirs,
684 2017). Such erosion could locally increase fan slope and potentially also encourage further
685 gully erosion headward. Thus, slope response after deglaciation will not only be related to
686 glacial debuitressing, causing glacial unloading and subsequent substrate cohesion loss,
687 but wider landscape adjustment to non-glacial conditions, independent of paraglacial stress
688 release (Cossart et al., 2008).

689 The length of time by which a glacial landscape responds after glacier recession has been
690 described by Cruden and Hu (1993) using a theoretical exhaustion model. Starting from this
691 mathematical simulation, Ballantyne (1995) and Curry (1999) argued that debris-mantled
692 slopes complete their paraglacial cycle rapidly, in 50-200 years since deglaciation, and
693 achieve a final, stable, geomorphic state characterized by an upper zone of exposed
694 bedrock resulting from downslope sediment evacuation, a central zone where water flows
695 in a concentrated way and several coalescent alluvial fans at the hillslope base (Chorley
696 and Kennedy, 1971; Schrott et al., 2003). These studies were conducted for lateral moraines
697 (e.g. Fåbergstølsdalen and Bas Glacier d'Arolla's proglacial areas) that were not influenced
698 by other effects, including the effects of the progressive reworking of moraine material upon
699 underlying bedrock exposure. When perfect connectivity is reached at the geomorphic
700 system scale and all sediment sources have been exhausted, the paraglacial period may be

701 considered over. In such systems, sediment inputs may still occur but they become limited
702 to rockfalls linked to paraglacial and paraperiglacial processes (Mercier, 2008). In our case,
703 the two studied subsystems were located just below a moraine bastion that clearly acted as
704 a primary sediment source. Due to its persistence, it is logical to expect that the time needed
705 to achieve a perfect connection and to rework available unconsolidated sediments is longer.
706 In 1964, the hillslope was characterized by multiple buffers (or sinks). In 2009, after the
707 headward erosion gullies some of them were still present, especially on the moraine bastion
708 (Figure 19), and sediment reworking towards the alluvial fans continued to occur (Figures
709 12F and 13F). Once all the remaining buffers are eroded, additional time will be needed to
710 exhaust the newly activated sediment sources (Cossart, 2008). Thus, following Ballantyne
711 (2002a) and Cossart (2008), we are unable to predict the duration of the paraglacial period
712 in our study area using the equation formulated by Cruden and Hu (1993). This is because
713 both subsystems are still perturbed by base level change (i.e. alluvial fan basal erosion) and
714 headward erosion, which in combination unlock new sediment source areas and sediment
715 transfers in the form of secondary peaks.

716 717 4.2 The sediment cascade and hydrological connectivity changes following glacial 718 debuttressing

719
720 As identified in other cases (e.g. Cossart and Fort, 2008), at the beginning of our study the
721 sediment cascades associated with the subsystems were affected by several intermediate
722 sinks that obstructed sediment flux to the valley bottom (Figures 11) and diminished their
723 effective catchment areas (Harvey, 2002). These latter were composed of inherited glacial
724 landforms, including a discontinuous LIA ridge that partially breaks up the slope, as also
725 observed by others (e.g. Knight et al. 2007; Cossart and Fort, 2008; Lane et al., 2017), and
726 by barriers associated with interactions between paraglacial sediment reworking and local
727 topography (Cossart, 2008). Sediment connectivity is dynamic because it changes in
728 response to erosion and deposition, processes which itself regulates (Hugget, 2007; Fryirs,

729 2013). In our case, we have identified both connectivity-increasing and connectivity-
730 decreasing processes, in the form of erosion of gullies and deposition of alluvial fans
731 respectively (Figures 12, 13 and 19; Cossart and Fort, 2008). Progressive disappearance of
732 intermediate sinks allowed an increase of hydrological connectivity, with mean upslope
733 contributing area increasing in each subsystem by between +73.8% and +195.8%,
734 respectively (Figure 16, 17 and 19). This process appears to be linked to base level fall
735 following gradual glacier thinning (Figures 12 and 13) coupled with, as reported by Cossart
736 and Fort (2008) in their work on the Vallouise valley, the accumulation of meltwater coming
737 from a hanging glacier (de la Grande Lire, Figure 1) promoting pronounced gullying. Our
738 results therefore confirm the conclusions of Lane et al. (2017) that gullying can be an
739 important process in breaching features that disconnect downslope sediment flux, such as
740 moraine ridges. Increases in connectivity have a second effect: not only do they allow flux
741 more readily through a point in the landscape; they can also reorganize drainage basin areas
742 upstream, potentially increasing (or decreasing) upslope contributing area and in turn
743 increasing (or decreasing) erosion potential (Figure 19; Cossart, 2008; Fryirs, 2013; Bracken
744 et al., 2015). In 2009, we reported that increases in accumulated area at sampled sites
745 initially acting as buffers were between $2.1 \times 10^3 \text{ m}^2$ and $7.0 \times 10^3 \text{ m}^2$ (Figure 19 and table
746 8). At the LIA limit no increases occurred suggesting that in 1964 the LIA moraine had
747 already been breached (Figure 19).

748

749 In parallel to the fact that gullying is the main driver that increases access to upslope
750 sediment source via the erosion of buffers, our results also show that if headward erosion
751 becomes too intense, the regions close to the gully channel can experience a reduction of
752 their upslope contribution area and become less connected (Figure 18). The geomorphic
753 evolution of the subsystems suggests that gully channels had high erosion, especially
754 between 1970 and 1995, which established a well-defined gully network (Figures 12 and

755 13). The main channel was characterized by the greatest accumulated area values ($> 10^9$
756 m^2) meaning that the connectivity was at its maximum. During the same period, areas with
757 lower upslope contributing area (10^2 to $10^4 m^2$) clearly increased in area (by +16% for SS1
758 and +9.4% for SS2) suggesting that some regions have been decoupled and that their
759 contribution to the downstream transport of sediment is strongly reduced (Figure 18).
760 Following a geomorphological analysis, these are primarily gully sidewalls and patches of
761 exposed bedrock, but it is also possible that gully capture elsewhere occurred to reduce the
762 drainage through these sites (Figures 12 and 13). This may explain the fall in upslope
763 contributing area at the moraine bastion ridge between 1964 and 2009 (XIII | Figure 19).
764 Connectivity in these areas could be enhanced and re-established only if some depositional
765 events were triggered, such as gully sidewall collapses or debris flow deposition, as
766 occurred in 2009 leading to a reconfiguration of the gully network (Figures 12, 13 and 18;
767 Curry et al., 2009; Eyles et al., 1988). This is a clear observation that gullying does not only
768 lead to increases in sediment connection; erosion to bedrock may lead to the formation of
769 sinks if the bedrock topography allows it, reducing connection. As Cossart (2008) observed,
770 the evolution of connectivity on hillslopes can lead to morphological changes that may both
771 maintain and reduce connectivity according to their setting with respect to sediment sources.
772 Alluvial fans are the final accumulation zones where mass movements deposit reworked
773 sediments because it is rare that debris flows triggered on sidewalls directly reach the alluvial
774 plain (Becht, 1995; Curry, 2000; Hilger et al., 2019), even if the question is debated as
775 sediment delivery to the main channel network in proglacial settings may be variable (Haas
776 et al., 2012). Schrott et al. (2006) studied alluvial fan buffering along a valley, and found a
777 clear relationship between deglaciation time and fan effectiveness in storing sediments. In
778 the lower parts of deglaciated catchments, alluvial fans reduced hillslope to valley floor
779 connection because stabilization also resulted in progressive revegetation. In contrast, in
780 the upper parts of deglaciated catchments, even if alluvial fans intercept down-wasting

781 sediments and reduce the overall connectivity, their sink effect is less pronounced due to
782 the abundant amounts of unconsolidated glacial sediment prone to be reworked. The
783 alluvial fans, for the most recent dates reported here, remain poorly vegetated suggesting
784 that they may still be active. However, even without vegetation, alluvial fans have reduced
785 slopes (Figure 11), tend to be diffusive in hydrological terms and are commonly well-drained
786 (Figures 15 and 19), all of which will lead to their effectiveness in decoupling valley side
787 slopes from the stream bottom (Fryirs and Brierley, 1999; Harvey, 2001; Lane et al., 2017).
788 For instance, by 2009 no more obstacles influenced connectivity our subsystems but it is
789 clear that the diffusive flow, mainly induced by gradient reduction, may encourage deposition
790 before sediments reach the valley bottom (Figure 15 and III and IX in Figure 19). This
791 observation concerns especially SS2, in which the gully is less channelized on the alluvial
792 fan compared to SS1 (Gomez and Purdie, 2018). It may also explain the different behavior
793 in terms of accumulated area evolution (deposition of $2.7 \times 10^4 \text{ m}^2$ for sample III and erosion
794 of $5 \times 10^{-3} \text{ m}^2$ for sample IX, Figure 19 and table 7) between the two subsystems.

795

796 **5. Conclusions**

797

798 Observations of the historical geomorphological changes that occur during the glacial
799 debuitressing phase of a retreating, temperate, Alpine valley glacier allowed us to quantify
800 the evolution of two subsystems associated with valley side slopes. Both were below a Little
801 Ice Age formed lateral moraine. We quantified this evolution in terms of historical surface
802 change and hydrological sediment connectivity.

803 Due to gully development with erosion rates of -10 mm/year and -1002 mm/year, between
804 1964 and 2009 the two subsystems evolved into a sediment cascade resembling that of a
805 torrent system: an upper source zone, related to a moraine bastion and moraine material
806 covering the valley sidewall; a gullied channel mainly activated during high magnitude
807 rainfall events; and, finally, a lower accumulation zone consisting of alluvial fans and the

808 proglacial alluvial plain (with deposition rates of +21 mm/year and +298 mm/year). The
809 evolution of these two subsystems then caused feedbacks that in turn impacted the
810 evolution of their connectivity. SS1 evolved through the removal of intermediate sinks and an
811 increase in connectivity (mean upslope contributing area value increased of 74%). Gully
812 extension to the moraine bastion above maintained sediment supply and prevented erosion
813 to bedrock and the development of bedrock-related steps that would have disconnected
814 sediment flux. SS2, also experienced local increases in connectivity (increase of the mean
815 accumulated area of 195%), but resulting increases in upstream sediment supply were
816 insufficient to prevent denudation to bedrock, resulting in disconnection. In both cases,
817 fluvially down-wasted sediments deposited at the hillslope base generated diffuse flow and
818 disconnection, probably linked to the absence of a well-defined channelized stream.

819 We confirmed that gully headward erosion is the most important geomorphological agent to
820 improve connectivity in this kind of environment, reaching even more upslope sediment
821 sources and eroding buffers on its path (vertical connectivity). We quantified that, at the
822 hillslope scale between 1964 and 2009, an area of 24810 m² (ca. +3%) had been “activated”.
823 However, we also highlighted that if incision is too intense, regions located close to the gully
824 network (16% of the total area for SS1 and 9.4% for SS2) experience reductions in upslope
825 contributing area (lateral connectivity). The main causes could be linked to gully sidewall
826 formation, patches of bedrock exposure and gully capture events.

827 Thus, it is likely that the paraglacial phase contains subsystems that are responding to
828 deglaciation at different rates, according to the extent to which erosion results in negative
829 feedbacks that reduce sediment flux. This is a local effect, meaning that the prediction of
830 the geomorphic response to debuttreassing is context specific. We highlighted that in complex
831 geomorphic systems, external sediment sources, in our case the moraine bastion, certainly
832 perturb the evolution of the subsystems by promoting inputs of upslope originating sediment
833 and forming secondary peaks (ex. following the activation of new sediment sources),

834 prolonging the length of the paraglacial period. This is a hypothesis that merits further
835 testing.

836

837 **Acknowledgments**

838

839 This research did not receive any specific grant from funding agencies in the public,
840 commercial, or not-for-profit sectors. A special thanks to Gilles Antoniazza and Dr.
841 Christophe Lambiel for the aid during the fieldwork and for their helpful advices. Dr. Markus
842 Stoffel and three anonymous reviewers are thanked for their very constructive and useful
843 comments on a previous version of this manuscript.

844

845 **6. References**

846

- 847 Arnold, N.S., 2010. A new approach for dealing with depressions in digital elevation models
848 when calculating flow accumulation values. *Prog. Phys. Geography: Earth and*
849 *Environ.*, 34, 781-609.
- 850 Ballantyne, C.K. and Benn, D.I., 1994. Paraglacial slope adjustment and resedimentation
851 following glacier retreat, Fabergstolsdalen, Norway. *Arc. and Alp. Res.*, 26, 255-
852 169.
- 853 Ballantyne, C.K., 1995. Paraglacial debris cone formation on recently deglaciated terrain.
854 *The Holocene*, 5, 25-33.
- 855 Ballantyne, C.K., 2002a. Paraglacial geomorphology. *Quaternary Sci. Revs.* 21, 1935-2017.
- 856 Ballantyne, C.K., 2002b. A general model of paraglacial landscape response. *The Holocene*,
857 12, 371-76.
- 858 Bakker, M. and Lane, S.N., 2017. Archival photogrammetric analysis of river-floodplain
859 systems using Structure from Motion (SfM) method. *Earth Surf. Process. Landf.*,
860 42, 1274-1286.
- 861 Bauder, A., Funk, M., Huss, M., 2007. Ice-volume changes of selected glaciers in the Swiss
862 Alps since the end of the 19th century. *Ann. of Glaciol.*, 46, 145-149.
- 863 Beawert, H. and Morche, D., 2014. Coarse sediment dynamics in a proglacial fluvial system
864 (Fagge River, Tyrol). *Geomorphology*, 218, 88-97.
- 865 Becht, M., 1995. Slope erosion processes in the Alps, in: Slaymaker, O. (Ed.), *Steepland*
866 *Geomorphology*. John Wiley and Sons, Chichester, pp.45-61.
- 867 Borselli, L., Cassi, P., Torri, D., 2008. Prologomena to sediment and flow connectivity in the
868 landscape: A GIS and field numerical assessment. *Catena*, 75, 268-277.
- 869 Bracken, L.J., Turnbull, L., Wainwright, J., Bogaart, P., 2015. Sediment connectivity: a
870 framework for understanding sediment transfer at multiple scales. *Earth Surf.*
871 *Process. Landf.*, 40, 177-188.
- 872 Brardinoni, F. and Hassan, M.A., 2006. Glacial erosion, evolution of river long profiles, and
873 the organization of processes domains in mountain drainage basins of coastal
874 British Columbia. *J. of Geophysical Res.*, 111, F01013, 1-12.

- 875 Brasington, J., Rumsby, B.T., Mcvey, R.A., 2003. Monitoring and modeling morphological
876 change in a braided gravel-bed river using high resolution GPS-based survey.
877 *Earth Surf. Process. Landf.*, 25, 973-990.
- 878 Carrivick, J.L. and Rushmer, E.L., 2009. Inter-and intra-catchment variation in proglacial
879 geomorphology: an example from Franz Josef Glacier and Fox Glacier, New
880 Zealand. *Arct., Antarc., and Alp. Res.*, 41, 18-36.
- 881 Carrivick, J.L., Gailhausen, M., Warburton, J., Dickson, N.E., Carver, S.J., Evans, A.J.,
882 Brown, L.E., 2013. Contemporary geomorphological activity throughout the
883 proglacial area of an alpine catchment. *Geomorphology*, 188, 83-95.
- 884 Carrivick, J.L., Berry, K., Geilhausen, M., James, W.H.M., Williams, C., Brown, L.E., Rippin,
885 D.M., Carver, S.J., 2015. Decadal-scale changes of the ödenwinkelkees central
886 Austria, suggest increasing control of topography and evolution towards steady
887 state. *Geografiska Annaler*, 97, 543-562.
- 888 Carrivick, J.L. and Heckmann, T., 2017. Short-term geomorphological evolution of proglacial
889 systems. *Geomorphology*, 287, 3-28.
- 890 Carrivick, J.L., Heckmann, T., Turner, A., Fischer, M., 2018. An assessment of landform
891 composition and functioning with the first proglacial system dataset of the central
892 European Alps. *Geomorphology*, 321, 117-128.
- 893 Cavalli, M., Trevisani, S., Comiti, F., Marchi, L., 2013. Geomorphometric assessment of
894 spatial sediment connectivity in small Alpine catchments. *Geomorphology*, 188,
895 31-41.
- 896 Chorley, R.J. and Kennedy, B.A., 1971. *Physical geography: A system approach*. Prentice-
897 Hall International Inc., London.
- 898 Church, M. and Ryder, J.M., 1972. Paraglacial sedimentation: a consideration of fluvial
899 processes conditioned by glaciation. *Geological Society of America Bulletin*, 83,
900 3059-3072.
- 901 Cossart, E., 2008. Landform connectivity and waves of negative feedbacks during the
902 paraglacial period, a case study: the Tabus subcatchment since the end of the
903 Little Ice Age (massif des Ecrins, France). *Géomorphologie: relief, processus,*
904 *environnement*, 14, 249-260.
- 905 Cossart, E. and Fort, M., 2008. Sediment release and storage in early deglaciated areas:
906 Towards an application of the exhaustion model from the case of Massif des
907 Ecrins (French Alps) since the Little Ice Age. *Nor. J. of Geography*, 62, 115-131.
- 908 Cossart, E., Braucher, R., Fort, M., Bourlès, D.L., Carcaillet, J., 2008. Slope stability in
909 relation to glacial debuitressing in alpine areas (Upper Durance catchment,
910 southeastern France): Evidence from field data and ¹⁰Be cosmic ray exposure
911 ages. *Geomorphology*, 95, 3-26.
- 912 Cruden, D.M. and Hu, X.Q., 1993. Exhaustion and steady-state models for predicting
913 landslide hazards in the Canadian Rocky Mountains. *Geomorphology*, 8, 279-
914 285.
- 915 Curry, A.M., 1999. Paraglacial modification of slope form. *Earth Surf. Process. Landf.*, 24,
916 1213-1228.
- 917 Curry, A.M., 2000. Observation on the distribution of paraglacial reworking of glacial drift
918 in western Norway. *Norsk Geografisk Tidsskrift – Nor. J. of Geography*, 54, 139-
919 147.
- 920 Curry, A.M., Cleasby, V., Zukowskyj, P., 2006. Paraglacial response of steep, sediment-
921 mantled slopes to post-'Little Ice Age' glacier recession in the central Swiss Alps.
922 *J. Quaternary Sci.*, 21, 211-225.
- 923 Curry, A.M., Sands, T.B., Porter, P.R., 2009. Geotechnical controls on a steep lateral
924 moraine undergoing paraglacial slope adjustment. Geological Society Special
925 Publication, 320, 181-197.

- 926 Deluigi, N., Lambiel, C., Kanevski, M., 2017. Data-driven mapping of the potential mountain
927 permafrost distribution. *Sci. of the Total Environ.*, 590-591, 370-380.
- 928 Davis, T.R.H., Warburton, J., Dunning, S.A., Bubeck, A.A.P., 2013. A large landslide event
929 in a post-glacial landscape: rethinking glacial legacy. *Earth Surf. Process. Landf.*,
930 38, 1261-1268.
- 931 Derose, R.C., Gomez, B., Marden, M., Trustum, N.A., 1998. Gully erosion in Mangatu forest,
932 New Zealand, estimated from digital elevation models. *Earth Surf. Process.*
933 *Landf.*, 23, 1045-1053.
- 934 Evans, S.G. and Clague, J.J., 1994. Recent climatic change and catastrophic geomorphic
935 processes in mountain environments. *Geomorphology*, 10, 107-128.
- 936 Fischer, M., Huss, M., Bardoux, C., Hoelzle, M., 2014. The new Swiss Glacier inventory
937 SGI2010: Relevance of using high-resolution source data on areas dominated by
938 very small glaciers. *Arct., Antarc., and Alp. Res.*, 46, 933-945.
- 939 Fischer, M., Huss, M., Hoelzle, M., 2015. Surface elevation and mass changes of all Swiss
940 glaciers 1980-2010. *The Cryosphere*, 9, 525-540.
- 941 Fryirs, K. and Brierley, G.J., 1999. Slope-channel decoupling in Wolumla catchment, New
942 South Wales, Australia: the changing nature of sediment sources following
943 European settlement. *Catena*, 35, 41-63.
- 944 Fryirs, K., 2013. (Dis)Connectivity in catchment sediment cascades: a fresh look at the
945 sediment delivery problem. *Earth Surf. Process. Landf.*, 38, 30-46.
- 946 Fonstad, M.A., Dietrich, J.T., Courville, B.C., Jensen, J.L., Carbonneau, P., 2013.
947 Topographic structure from motion: a new development in photogrammetric
948 measurement. *Earth Surf. Process. Landf.*, 38, 421-430.
- 949 Gabbud, C., Micheletti, N., Lane, S.N., 2016. Response of a temperate Alpine valley glacier
950 to climate change at a decadal scale. *Geografiska Annaler*, 98, 81-95.
- 951 Glaciers Monitoring in Switzerland (GLAMOS), 2016. Glacier d'Otemma, Bagnes (VS).
952 Swiss glacier monitoring network. [www.swiss-
953 glaciers.glaciology.ethz.ch/glaciers/otemma](http://www.swiss-glaciers.glaciology.ethz.ch/glaciers/otemma) (accessed September 2018).
- 954 Gomez, C. and Purdie, H., 2018. Point cloud technology and 2D computational flow dynamic
955 modeling for rapid hazards and disaster risk appraisal on Yellow Creek fan,
956 Southern Alps of New Zealand. *Prog. Earth Planet. Sci.*, 5.
- 957 Haas, F., Heckmann, T., Hilger, L., Becht, M., 2012. Quantification and modelling of debris
958 flows in the proglacial area off he Gepatschferner/Autria using ground-based
959 LiDAR, in: Collins, A.L., Golosov, V., Horowitzm A.J., Lu, X., Stone, M., Walling,
960 D.E., Zhang, X. (Eds.), *Erosion and sediment yields in the changing environment*,
961 IAHS Publications, Wallingford, pp. 293-302.
- 962 Haeberli, W., Wegmann, M., Vonder Mühl, D., 1997. Slope stability problems related to
963 glacier shrinkage and permafrost degradation in the Alps. *Ecologiae Geologicae*
964 *Helveticae*, 90, 407-414.
- 965 Haeberli, W. and Beniston, M., 1998. Climate change and its impacts on glaciers and
966 permafrost in the Alps. *Ambio*, 27, 258-265.
- 967 Hancock, G.R., 2006. The impact of different gridding methods on catchment
968 geomorphology and soil erosion over long timescales using a landscape
969 evolution model. *Earth Surf. Process. Landf.*, 31, 1035-1050.
- 970 Harrison, S. and Winchester, V., 1997. Age and nature of paraglacial debris cones along the
971 margins of the San Rafael glacier, Chilean Patagonia. *The Holocene*, 7, 481-487.
- 972 Harvey, A.M., 1977. Coupling between hillslope gully systems and stream channels in the
973 Howgill Fells, northwest England: temporal implications. *Géomorphologie: relief,
974 processus, environnement*, 3, 3-19.

- 975 Harvey, A.M., 2001. Coupling between hillslopes and channels in upland fluvial systems:
976 implications for landscape sensitivity illustrated from the Howgill Fells, northwest
977 England. *Catena*, 42, 225-250.
- 978 Harvey, A.M., 2002. Effective timescale of coupling within fluvial systems. *Geomorphology*,
979 44, 175-201.
- 980 Heckmann, T., McColl, S., Morche, D., 2016. Retreating ice: research in proglacial areas
981 matters. *Earth Surf. Process. Landf.*, 41, 271-276.
- 982 Heritage, G.L., Milan, D.J., Large, A.R.G., Fuller, I.C., 2009. Influence of survey strategy
983 and interpolation model on DEM quality. *Geomorphology*, 112, 334-344.
- 984 Hilger, L., Dusik, J.-M., Heckmann, T., Haas, F., Glira, P., Pfeifer, N., Vehling, L., Rohn, J.,
985 Morche, D., Baewert, H., Stocker-Waldhuber, M., Kuhn, M., Becht, M., 2019. A
986 sediment budget of the Upper Kaunertal, in: Heckmann, T., Morche, D. (Eds.),
987 *Geomorphology of Proglacial Systems. Geography of the Physical Environment*.
988 Springer, Cham, pp. 289-312.
- 989 Holmes, K.W., Chadwick, O.A., Kyriakidis, P.C., 2000. Error in a USGS 20-meter digital
990 elevation model and its impacts on terrain modelling. *J. of Hydrol.*, 233, 154-173.
- 991 Holmgren, P., 1994. Multiple flow direction algorithms for runoff modelling in grid based
992 elevation models: an empirical evaluation. *Hydrol. Process.*, 8, 327-333.
- 993 Hugenholz, C.H., Moorman, B.J., Barlow, J., Wainstein, P.A., 2008. Large-scale moraine
994 deformation at the Athabasca Glacier, Jasper National Park, Alberta, Canada.
995 *Landslides*, 5, 251-260.
- 996 Hugget, R.J., 2007. *Foundamentals of Geomorphology*. Routledge: London.
- 997 Immerzeel, W.W., Kraaijenbrink, P.D.A., Shea, J.M., Shrestha, A.B., Pellicciotti, F.,
998 Bierkens, M.F.P., de Jong, S.M. (2014). High-Resolution monitoring of Himalayan
999 glacier dynamics using unmanned aerial vehicles. *Remote Sens. Environ.*, 150,
1000 93-103.
- 1001 Javernick, L., Brasington, J., Caruso, B., 2014. Modeling the topography of shallow bridged
1002 rivers using Structure-from-Motion photogrammetry. *Geomorphology*, 213, 166-
1003 182.
- 1004 Kääh, A. and Vollmer, M., 2000. Surface Geometry, Thickness Changes and Flow Fields on
1005 Creeping Mountain Permafrost: Automatic Extraction by Digital Image Analysis.
1006 *Permafr. and Periglac. Process.*, 11, 315-326.
- 1007 Knight, P.G., Jennings, C.E., Waller, R.I., Robinson, Z.P., 2007. Changes in ice-margin
1008 processes and sediment routing during ice-sheet advance across a marginal
1009 moraine. *Geografiska Annaler*, 89, 203-215.
- 1010 Küng, O., Strecha, C., Beyeler, A., Zuffrey, J.C., Floreano, D., Fua, P., Gervais, F., 2011.
1011 The Accuracy of Automatic Photogrammetric Techniques on Ultra-Light UAV
1012 Imagery. *Int. arch. of the Photogramm., Remote Sens. and Spat. Inf. Sci.*, 38,
1013 125-130.
- 1014 Lambiel, C. and Reynard, E., 2001. Regional modelling of present, past and future potential
1015 distribution of discontinuous permafrost based on a rock glacier inventory in the
1016 Bagnes Hérémece area (Western Swiss Alps). *Norsk Geografisk Tidsskrift –*
1017 *Nor. J. of Geography*, 55, 219-224.
- 1018 Lambiel, C., Maillard, B., Kummert, B., Reynard, E., 2016. Geomorphology of the Hérens
1019 valley (Swiss Alps). *J. of Maps*, 12, 160-172.
- 1020 Lambiel, C. and Talon, P., in press. Les glaciers du Haut Val de Bagnes au Petit Age
1021 Glaciaire. *Annales valaisannes, Actes du colloque Giétro 1818*, Martigny.
- 1022 Lane, S.N., Richards, K.S., Chandler, J.H., 1993. Developments in photogrammetry: the
1023 geomorphological potential. *Prog. Phys. Geography*, 13, 306-328.
- 1024 Lane, S.N., Chandler, J.H., Richards, K.S., 1994. Developments in monitoring and modeling
1025 small-scale river bed topography. *Earth Surf. Process. Landf.*, 19, 349-368.

- 1026 Lane, S.N., 1998. The use of digital terrain modeling in the understanding of dynamic river
1027 systems, in: Lane, S.N., Richards, K.S., Chandler, J.H. (Eds), *Landform*
1028 *Monitoring, Modelling, and Analysis*. John Wiley and Sons, Chichester, pp. 311-
1029 342.
- 1030 Lane, S.N., Westaway, R.M., Hicks, D.M., 2003. Estimation of erosion and deposition
1031 volumes in a large, gravel-bed, braided river using synoptic remote sensing. *Earth*
1032 *Surf. Process. Landf.*, 28, 181-198.
- 1033 Lane, S.N., Reid, S.C, Westaway, R.M., Hicks, D.M., 2004. Remotely sensed topographic
1034 data for river research: the identification, explanation and management of error,
1035 in: Kelly, R.E.J., Drake, N.A., Barr, S.L. (Eds), *Spatial Modelling of the Terrestrial*
1036 *Environment*. John Wiley and Sons, Chichester, pp. 113-136.
- 1037 Lane, S.N., Widdison, P.E., Thomas, R.E., Ashworth, P.J., Best, J.L., Lunt, I.A., Sambrook
1038 Smith, G.H., Simpson, C.J., 2010. Quantification of braided river channel change
1039 using archival digital image analysis. *Earth Surf. Process. Landf.*, 35, 971-985.
- 1040 Lane, S.N., Bakker, M., Gabbud, C., Micheletti, N., Saugy, J. N., 2017. Sediment export,
1041 transient landscape response and catchment-scale connectivity following rapid
1042 climate warming and Alpine glacier recession. *J. Geomorph.*, 227, 210-227.
- 1043 Lane, S.N., Gabbud, C., Micheletti, N., 2018. Reconstructing sediment connection in Alpine
1044 landscapes undergoing rapid glacier recession. EU COST Meeting, Connecteur,
1045 26-28 March, Venice.
- 1046 Laute, K. and Beylich, A.A., 2012. Influences of the Little Ice Age glacier advance on hillslope
1047 morphometry and development in paraglacial valley systems around the
1048 Jostedalbreen ice cap in Western Norway. *Geomorphology*, 167, 51-69.
- 1049 Laute, K. and Beylich, A.A., 2013. Holocene hillslope development in glacially formed valley
1050 systems in Nordfjord, western Norway. *Geomorphology*, 188, 12-30.
- 1051 Laute, K. and Beylich, A.A., 2014. Environmental controls, rates and mass transfers of
1052 contemporary hillslope processes in the headwaters of two glacier-connected
1053 drainage basins in western Norway. *Geomorphology*, 216, 93–113.
- 1054 Lisenby, P.E. and Fryirs, K.A., 2017. Sedimentologically significant tributaries: catchment-
1055 scale controls on sediment (dis)connectivity in the Lockyer Valley, SEQ,
1056 Australia. *Earth Surf. Process. Landf.*, 42, 1493-1504.
- 1057 McColl, S., 2012. Paraglacial rock-slope stability. *Geomorphology*, 153, 1-16.
- 1058 McColl, S.T. and Davis, T.R.H., 2013. Large ice-contact slope movements: glacial
1059 buttressing, deformation and erosion. *Earth Surf. Process. Landf.*, 38, 1102-1115.
- 1060 Mercier, D., 1997. L'impact du ruissellement sur les moraines latérales du Glacier du Roi
1061 (Collentthonga, Spitzberg, 79°N). *Norv.*, 44, 549-566.
- 1062 Mercier, D., 2008. Paraglacial and paraperiglacial landsystems: concepts, temporal scales
1063 and spatial distribution. *Géomorphologie: relief, processus, environnement*,
1064 14(4), 223-233.
- 1065 Mercier, D., Etienne, S., Sellier, D., André, M.-F., 2009. Paraglacial gullying of sediment-
1066 mantled slopes: a case study of Colletthøgda, Kongsfjorden area, West
1067 Spitsbergen (Svalbard). *Earth Surf. Process. Landf.*, 34, 1772-1789.
- 1068 Micheletti, N., Lambiel, C., Lane, S.N., 2015a. Investigating decadal-scale geomorphic
1069 dynamics in an alpine mountain setting. *J. of Geophys. Res.: Earth Surf.*, 120,
1070 2155-2175.
- 1071 Micheletti, N., Lane, S.N., Chandler, J.H., 2015b. Application of archival aerial
1072 photogrammetry to quantify climate forcing of Alpine landscapes. *The*
1073 *Photogrammetric Records*, 30, 143-165.
- 1074 Micheletti, N., Chandler, J.H., Lane, S.N., 2015c. Structure from Motion (SfM)
1075 photogrammetry, in Cook, S.J., Clarke, L.E., Nield, J.M. (Eds), *Geomorphological*
1076 *techniques*. British Society for Geomorphology, London, pp.1-12.

- 1077 Miller, P., Mills, J., Edwards, S., Bryan, P., Marsh, S., Mitchell, H., Hopps, P., 2008. A robust
1078 surface matching technique for coastal geohazard assessment and
1079 management. *ISPRS J. of Photogramm. and Remote Sens.*, 65, 529-542.
- 1080 Mölg, N. and Bolch, T., 2017. Structure-from-Motion using historical aerial images to analyse
1081 changes in glacier surface elevation. *Remote sens.*, 9, 1021-1038.
- 1082 Moore, I.D., Grayson, R.B., Ladson, A.R., 1991. Digital terrain modeling: a review of
1083 hydrological, geomorphological and biological applications. *Hydrol. Process.*, 5,
1084 3-90.
- 1085 Paul, F., Kääb, A., Maisch, M., Kellenberger, T., Haeberli, W., 2004. Rapid disintegration of
1086 Alpine glaciers observed within satellite data. *Geophys. Res. Lett.*, 31.
- 1087 Porter, P.R., Vatne, G., Ng, F., Irvine-Flynn, T.D.L., 2010. Ice-marginal sediment delivery to
1088 the surface of a high-Arctic glacier: Austere Broggerbreen, Svalbard. *Geografiska
1089 Annaler*, 92, 437-449.
- 1090 Quinn, P., Beven, K., Chevallier, P., Planchon, O., 1991. The prediction of hillslope flow
1091 paths for distributed hydrological modelling using digital terrain models. *Hydrol.
1092 Process.*, 5, 59-79.
- 1093 Rieger, W., 1998. A phenomenon-based approach to upslope contributing area and
1094 depressions in DEMs. *Hydrol. Process.*, 12, 857-872.
- 1095 Schiefer, E. and Gilbert, R., 2007. Reconstructing morphometric change in a proglacial
1096 landscape using historical aerial photography and automated DEM generation.
1097 *Geomorphology*, 88,167-178.
- 1098 Schrott, L., Hufschmidt, G., Hankammer, M., Hoffman, T., Dikau, R., 2003. Spatial
1099 distribution of sediment storage types and quantification of valley fill deposits in
1100 an alpine basin, Reintal, Bavarian Alps, Germany. *Geomorphology*, 55, 45-63.
- 1101 Schrott, L., Götz, J., Geilhausen, M., Morche, D., 2006. Spatial and temporal variability of
1102 sediment transfer and storage in an Alpine basin (Reintal valley, Bavarian Alps,
1103 Germany). *Geographica Helvetica*, 61, 191-200.
- 1104 Schwanghart, W. and Kuhn, N.J., 2010. TopoToolbox: a set of Matlab functions for
1105 topographic analysis. *Environ. Model. & Softw.*, 25, 770-781.
- 1106 Staines, K.E.H., Carrivick, J.L., Tweed, F.S., Evans, A.J., Russell, A.J., Johannesson, T.,
1107 Roberts, M., 2015. A multi-dimensional analysis of pro-glacial landscape change
1108 at Solheimajökull, Southern Iceland. *Earth Surf. Process. Landf.*, 40, 809-822.
- 1109 Warburton, J., 1990. An alpine proglacial fluvial sediment budget. *Geografiska Annaler*, 72,
1110 261-272.
- 1111 Watanabe, T., Dali, L., Shiraiwa, T., 1998. Slope denudation and supply of debris to cones
1112 in Landtang Himal, Central Nepal Himalaya. *Geomorphology*, 26, 185-197.
- 1113 Watanabe, Y. and Kawahara, Y., 2016. UAV photogrammetry for monitoring changes in
1114 river topography and vegetation. *Procedia Eng.*, 154, 317-325.
- 1115 Westoby, M.J., Brasington, J., Glasser, N.F., Hambrey, M.J., Reynolds, J.M., 2012.
1116 "Structure-from-Motion" photogrammetry: A low-cost, effective tool for
1117 geoscience applications. *Geomorphology*, 179, 300-314.
- 1118 Wheaton, J.M., Brasington, J., Darby, S.E., Sear, D.A., 2010. Accounting for uncertainty in
1119 DEMs from repeat topographic survey: improved sediment budgets. *Earth Surf.
1120 Process.Landf.*, 35, 136-156.
- 1121 Wulf, H., Bookhagen, B., Scherler, D., 2012. Climatic and geologic controls on suspended
1122 sediment flux in the Sutlej River Valley, western Himalaya. *Hydrol. Earth Syst.
1123 Sci.*, 16, 2193–2217.
- 1124 Zemp, M., Haeberli, W., Hoelzle, M., Paul, F., 2006. Alpine glaciers to disappear within
1125 decades?. *Geophys. Res. Lett.*, 33.
- 1126
1127

1128 Main characteristics of the aerial imagery used and associated camera/image parameters.

Year	Camera type	# images	Overlap [%]	Scale [1:x]	Scan resolution [μm]	Ground Pixel resolution [m]	Calibrated focal length [mm]
1964	Lens 29 11.5 AG	14	60	1:17700	21	0.37	115.29
1970	Lens 174 15 AG	9	60	1:8600	21	0.18	152.10
1977	Lens 3004 15 UAG II	17	60	1:8600	14	0.12	153.02
1983	Lens 13018 15/4 UAG	17	60	1:8600	14	0.12	153.37
1988	Lens 13018 15/4 UAG	18	60	1:8600	14	0.12	153.37
1995	Lens 13220 15/4 UAG-S	13	80	1:8600	14	0.12	152.52
2009	Lens 13220 15/4 UAG-S	14	80	1:19800	14	0.19	152.52

1129

1130

1131 4D's parameters and georeferencing error for stable zones marked with GCPs.

# GCPs	Tie-points per image	Resultant DEM resolution [m]	Theoretical precision [m]	Mean RMSE [m]	σ error [m]	
					X	Y
4	36341	1.998	±0.37	±0.457	±0.193	±0.245
5	81137	0.703	±0.18	±0.062	±0.01	±0.028
5	87125	0.608	±0.12	±0.104	±0.048	±0.190
8	92290	0.611	±0.12	±0.114	±0.085	±0.032
8	91906	0.631	±0.12	±0.369	±0.427	±0.093
8	93388	0.641	±0.12	±0.180	±0.156	±0.151
4	79913	1.651	±0.27	±0.081	±0.031	±0.023

Year	Error [m]			
	Before correction		After correction	
	\bar{z}	σ (precision)	\bar{z}	σ (precision)
1964	-18.8	±4.0	-0.9	±3.0
1970	-27.5	±4.9	-0.4	±0.5
1977	-9.9	±4.1	+0.4	±0.5
1983	-	-	-	-
1988	+4.9	±3.4	-0.1	±1.5
1995	+21.1	±6.8	-1.0	±1.3
2009	+1.3	±3.6	-0.6	±0.5

Table 3:

1135 error analysis based on stable zones.

1136

1137

1138

1139

1140

1141

1142

1143

1144

Year	Number of points in point clouds	Point cloud densities [pts/m ²]	Number of stable points used for registration	RMSE after registration [m]
1964	4'368'086	23.4	6	±1.0050
1970	12'348'682	66.2	12	±0.9051
1977	6'518'009	34.9	7	±0.5852
1983	8'715'575	46.3	-	-1153
1988	2'858'505	15.3	9	±0.1054
1995	3'045'655	16.3	8	±0.2855
2009	7'524'428	40.3	8	±0.1156

Table 4: Point clouds

1158 correlation and co-registration characteristics.

1159
1160
1161
1162
1163
1164
1165
1166
1167
1168
1169
1170
1171

1172 correlation and regression coefficient of the multi-regression model.

Year	r	Regression equation ($Z^p = a + bZ^0 + cZ^0$)		
		a	b	c
1964	0.9	36.5	-0.006	0.04
1970	0.92	-1.7x10 ³	0.002	0.007
1977	0.94	-1.7x10 ³	0.002	0.007
1983	-	-	-	-
1988	0.93	-1.1x10 ³	0.005	-0.028
1995	0.9	-269.4	0.003	-0.029
2009	0.9	-2.2x10 ³	0.004	-0.060

1182
1183

Year	68% LoD
1964-1970	±2.99
1970-1977	±1.70
1977-1983	±1.76

Table 6: Limits of Detection (LoD) for the DEMs of Difference.

1983-1988	± 1.74	Upslope contributing area (m ²)		
1988-1995	± 2.03	Date		
Location	± 1.78	1964	2009	Change
I		5.6×10^5	5.6×10^5	0
II		9.3×10^4	1.0×10^5	+7.0
III		7.3×10^4	1.0×10^5	+2.7
IV		8.0×10^4	8.0×10^4	0
V		9.0×10^4	3.0×10^5	+2.1
VI		2.0×10^4	9.0×10^4	+7.0
VII		1.0×10^2	1.0×10^4	+9.9
VIII		6.3×10^5	1.4×10^5	-4.9
IX		2.0×10^4	1.5×10^4	-5.0

- 1197
- 1198
- 1199
- 1200
- 1201
- 1202
- 1203
- 1204
- 1205
- 1206
- 1207
- 1208
- 1209
- 1210
- 1211
- 1212
- 1213
- 1214
- 1215
- 1216
- 1217
- 1218
- 1219

Upslope contributing area values (1964, 2009 and difference between the two dates) for the sampled locations highlighted in figures 15,

Cell value classes							
10^5	10^5-10^6	10^6-10^7	10^7-10^8	10^8-10^9	10^9-10^{10}	$10^{10}-10^{11}$	$10^{11}-10^{12}$
61 (9.7)	36224 (5795.8)	20603 (3296.5)	10093 (1614.9)	4891 (782.5)	1916 (306.6)	220 (35.2)	2 (0.32)
48 (5.7)	38342 (6134.7)	20314 (3250.2)	8541 (1366.6)	4152 (664.3)	1935 (309.6)	283 (45.3)	5 (0.8)
89 (1.2)	37709 (6033.4)	20137 (3221.9)	8516 (1362.6)	4259 (681.5)	1600 (256)	358 (57.3)	20 (3.2)
22 (9.5)	31167 (4986.7)	17048 (2727.7)	6879 (1100.6)	3415 (546.4)	1610 (257.6)	459 (73.4)	13 (2.1)
66 (4.6)	32836 (5253.8)	16635 (2661.6)	6816 (1090.6)	3273 (523.7)	1505 (240.8)	627 (100.3)	54 (8.64)

26 2.1)	25610 (4097.6)	16263 (2602.1)	6247 (999.5)	2978 (476.5)	1559 (249.4)	569 (91.1)	98 (15.7)
48 3.7)	41253 (6600.5)	16958 (2713.3)	6903 (1104.5)	4235 (677.6)	1968 (314.9)	336 (53.7)	1 (0.16)

1220 Difference in total number of cells per class and relative area (number of cells x [DEM resolution]², in brackets) for SS1.

1221

1222

1223 Difference in total number of cells per class and relative area (number of cells x [DEM resolution]², in brackets) for SS2.

Year	Cell value classes									
	0-10 ¹	10 ² -10 ³	10 ³ -10 ⁴	10 ⁴ -10 ⁵	10 ⁵ -10 ⁶	10 ⁶ -10 ⁷	10 ⁷ -10 ⁸	10 ⁸ -10 ⁹	10 ⁹ -10 ¹⁰	10 ¹⁰ -10 ¹¹
1964	18524 (2963.8)	24057 (3849.1)	35065 (5610.4)	43490 (6958.4)	41229 (6596.6)	28637 (4581.9)	13862 (2217.9)	5506 (880.9)	1601 (256.2)	1234 (40.2)
1970	14034 (2245.4)	22267 (3562.7)	35612 (5697.9)	45389 (7262.2)	15669 (2507.1)	32789 (5246.2)	15397 (2463.5)	4910 (785.6)	1318 (210.9)	1228 (105)
1977	15071 (2411.4)	22952 (3672.3)	34870 (5579.2)	44592 (7134.7)	44713 (7154.1)	33239 (5318.2)	15539 (2486.2)	5256 (840.9)	1175 (188)	1230 (91)
1983	26346 (4215.4)	31650 (5064)	39779 (6364.6)	42138 (6742.1)	35851 (5736.2)	23638 (3782.1)	11284 (1805.5)	4020 (643.2)	1183 (189.3)	1233 (13.9)
1988	19988 (3198.1)	28343 (4534.9)	39634 (6341.4)	46827 (7492.3)	43638 (6982.1)	30105 (4816.8)	14727 (2356.3)	4793 (766.9)	1478 (236.5)	1235 (26.9)
1995	19803 (3168.5)	29052 (4648.3)	40768 (6522.9)	48228 (7716.5)	43581 (6972.9)	30009 (4801.4)	13801 (2208.2)	5058 (809.3)	1513 (242.1)	1237 (102)
2009	13165 (2106.4)	35995 (5759.2)	38235 (6117.6)	51752 (8280.3)	51627 (8260.3)	37870 (6059.2)	14778 (2364.5)	4303 (688.5)	1240 (198.4)	1239 (7.4)

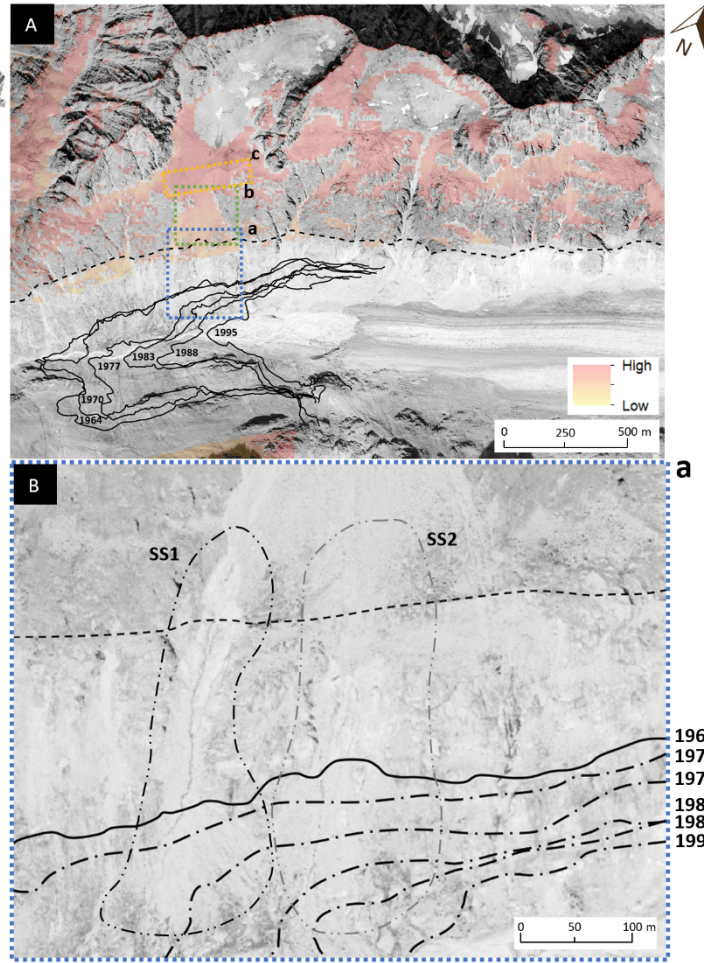


Figure 1: Location of the study area within the Glacier d'Otemma catchment (A) in 2009 and image of the valley sidewall in 2017 (B). Dashed line represents the supposed LIA right limit based on geomorphic investigation (location of moraine ridges and limit of vegetation). Squares in A highlight the LIA sector where our study is focused (a), the debris accumulation above the LIA limit (b), and the Glacier de la Grand Lire morainic bastion (c); solid lines refers to historical glacier outlines. Pixel colors refers to permafrost probability distribution (Deluigi et al., 2017). In B dashed solid and dash-dotted lines show the surface glacier thinning over time and the double dash-dotted lines represent SS1 and SS2.

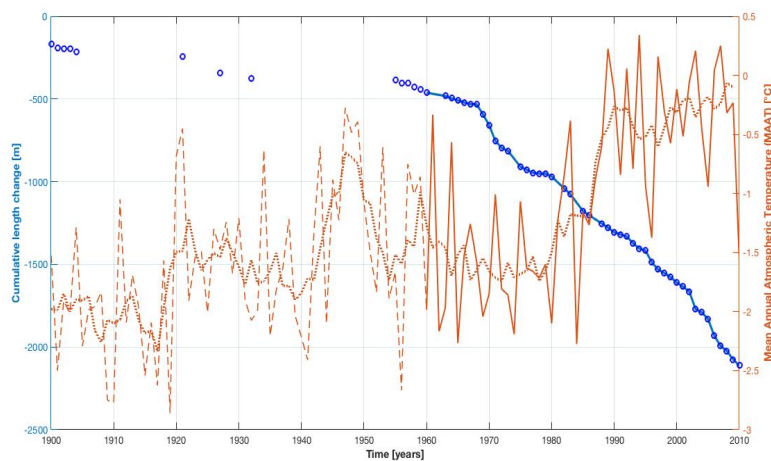
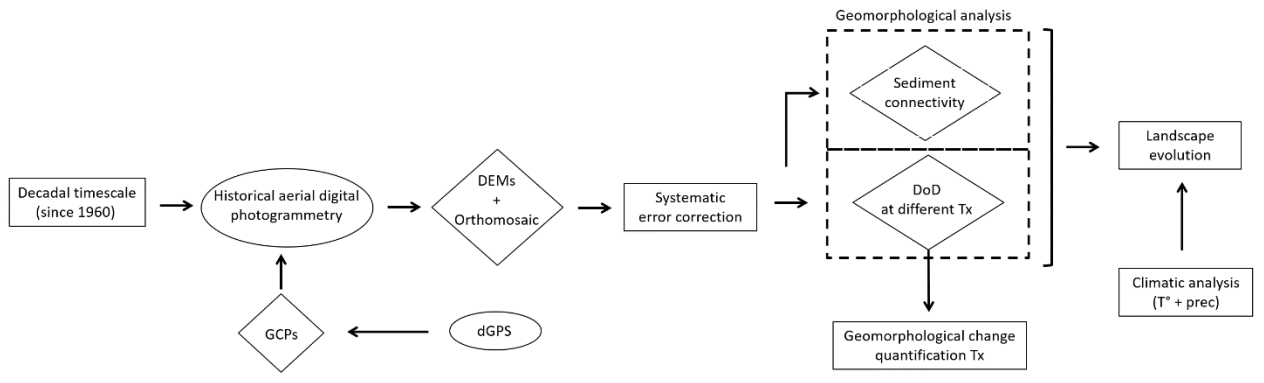


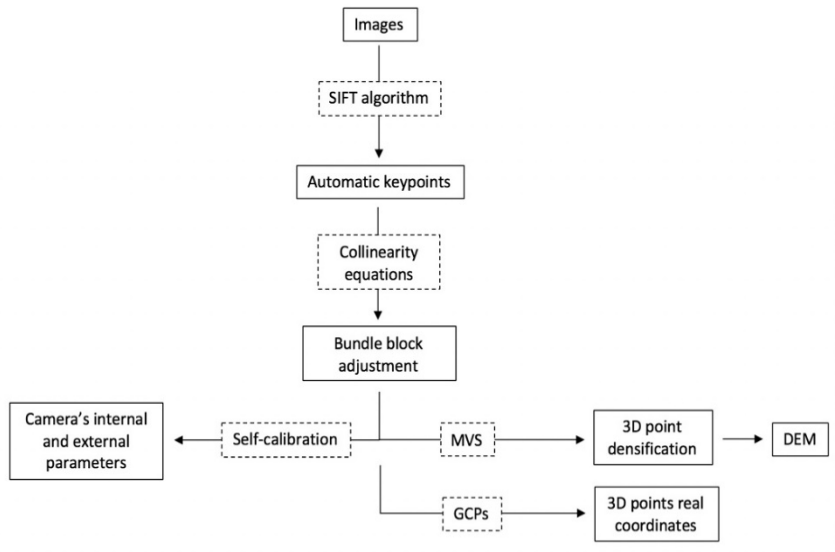
Figure 2: Glacier d'Otemma cumulative retreat in relation to the mean atmospheric annual temperature (MAAT) since 1900. Historical MAATs data refers to the Grand-Saint-Bernard climate station, located only 19 km from the study site at a similar altitude similar (2472 m a.s.l.) and all records are homogenized (the records are corrected by MétéoSuisse to remove influences of measurement method, small changes in station location, and changes in local climate influence such as urban development). The orange dotted line show the 5 years moving mean for MAAT.



1253
1254

Figure 3: Schematic view of the methodology.

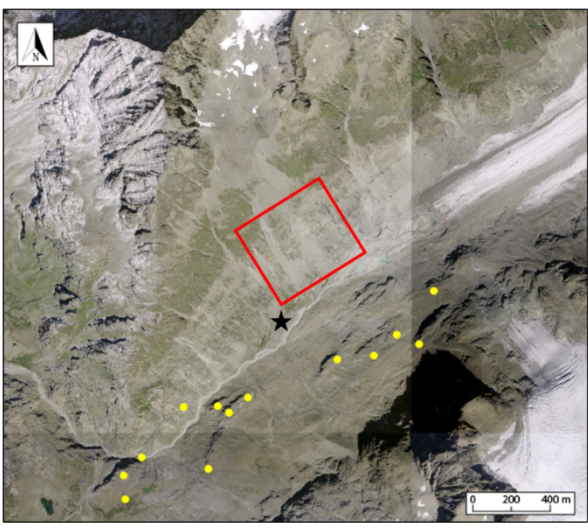
1255
1256



1257
1258

Figure 4: Schematic workflow for SfM photogrammetry, based on Fonstad et al., (2013).

1259



1260
1261
1262

Figure 5: Spatial distribution of GCPs (points), base station position (star) and location of the study area (square). Coordinates of base station (in CH1903+) are 2'597'518.2 N, 1'086'726.2 E. Source of background image: SwissTopo.

1263

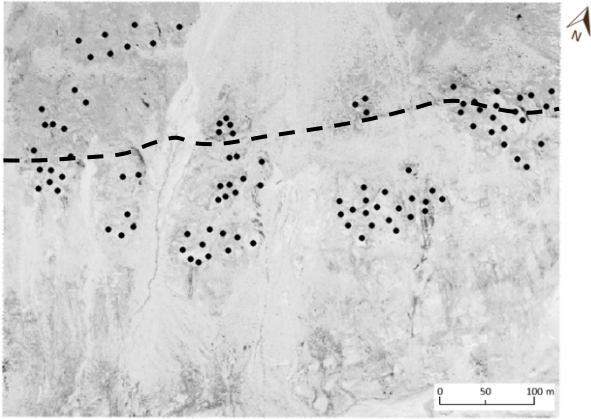


Figure 6: Location of the 98 Z points used to the detection of the systematic error and the computaion of LoDs (background image is dated 2009). Dashed line represents the supposed LIA limit based on geomorphic investigation (location of moraine ridges and limit of vegetation).

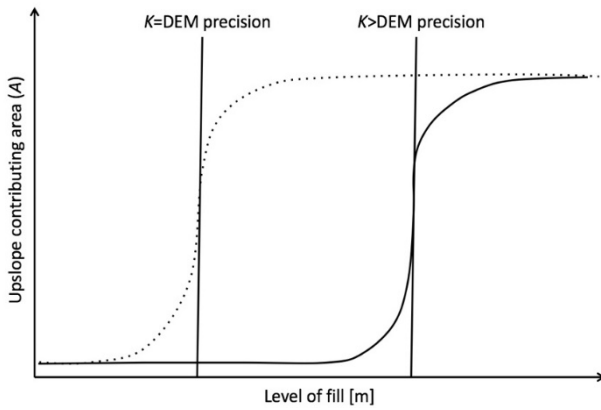


Figure 7: Hydrological sediment connectivity model for artificial (dotted line) and natural (dash-dotted line) disconnectivity in function of upslope contributing area (A), fill level and DEM precision (K) (Lane et al., 2018 – modified).

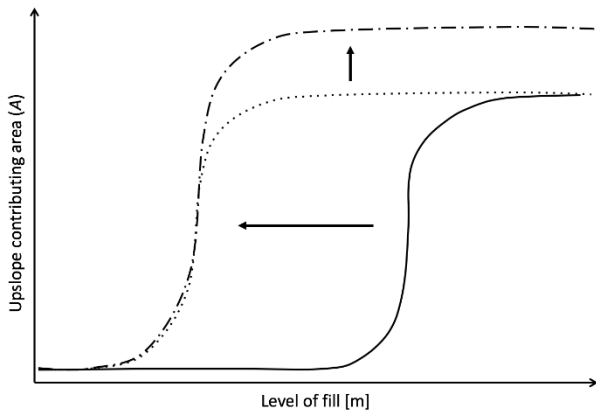


Figure 8: Hydrological sediment connectivity evolution ; base level fall and headward erosion propagation (dotted line) and upslope basin reorganization (dash-dotted line) (Lane et al., 2018 – modified).

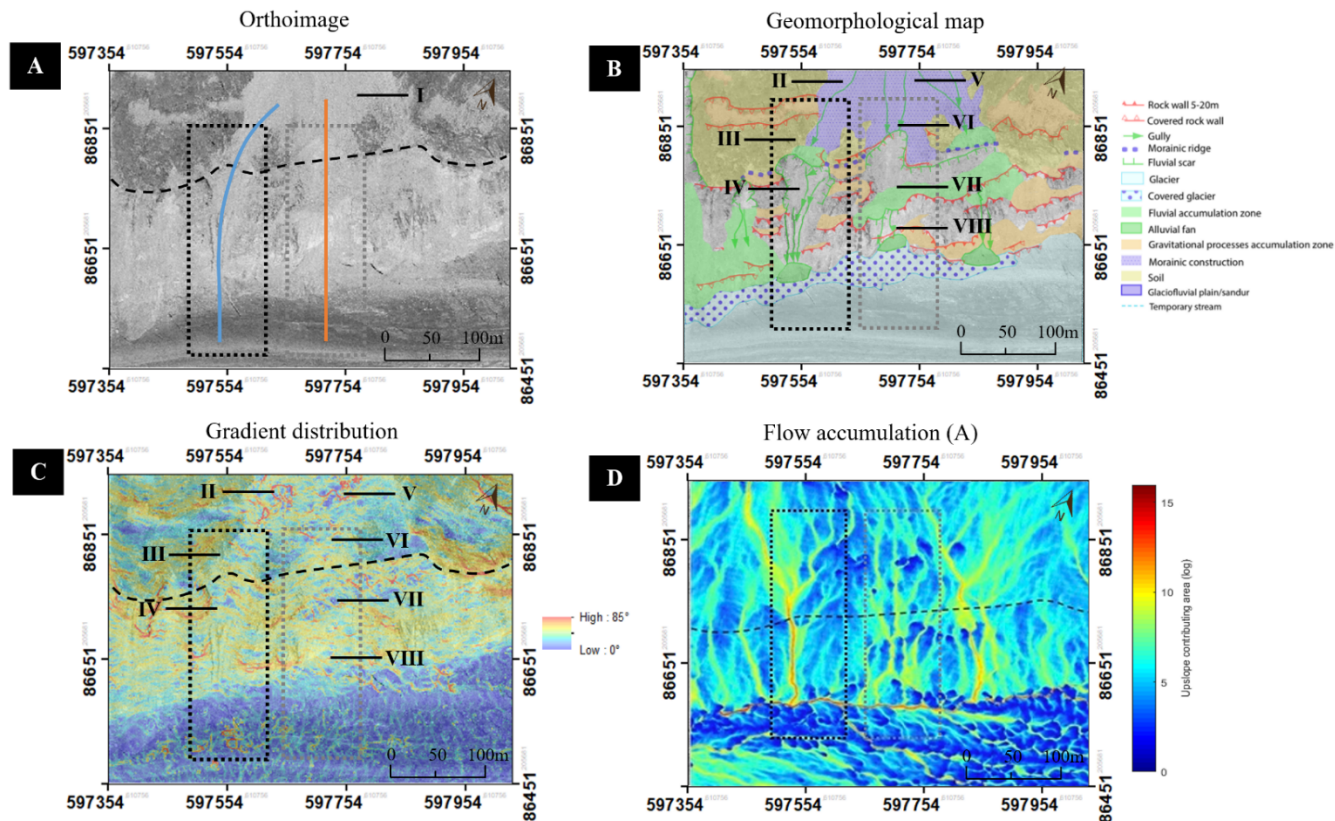


Figure 9: Geomorphological characteristics of the lateral moraine in 1964. A) Orthoimage highlighting the location of the elevation profile in Figure 10, B) geomorphological map using the University of Lausanne's classification (Lambiel et al., 2016), C) slope gradient and potential buffers, D) flow accumulation algorithm calculated with all pits filled with a threshold defined by the σ_{2009} (Table 3). Dotted squares refer to SS location while dashed line represent the supposed LIA limit.

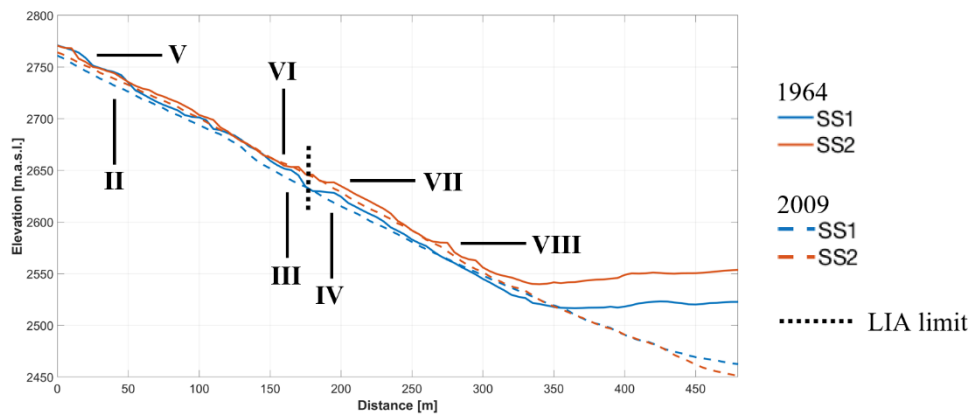


Figure 10: Gradient profiles of SS1 and SS2 in 1964 (solid lines) and 2009 (dashed lines). Spatial positions of the profiles are displayed in Figure 9 (for 1964) and Figure 10 (for 2009).

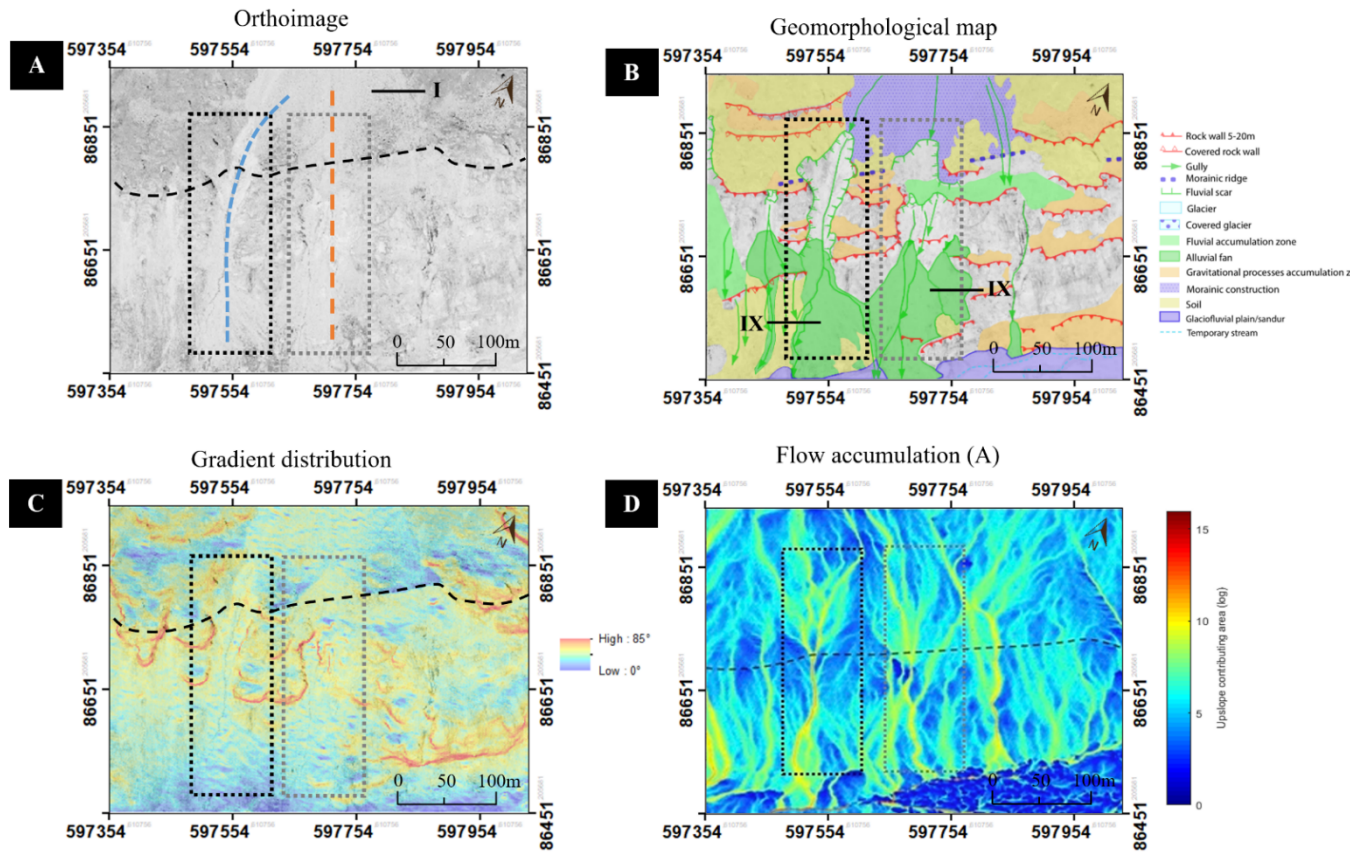


Figure 11: Geomorphologic characteristics of the lateral moraine in 2009. A) orthoimage highlighting the location of the elevation profiles in Figure 10, B) geomorphologic map using the University of Lausanne classification (Lambiel et al., 2016), C) slope gradient and potential buffers, D) flow accumulation algorithm calculated with all pits filled with a threshold defined by the (Table 3). Dotted squares refer to SS location while dashed line represent the supposed LIA limit.

1298
1299
1300
1301
1302

1303
1304
1305
1306
1307
1308
1309
1310
1311
1312
1313
1314
1315
1316
1317
1318
1319
1320
1321
1322
1323
1324

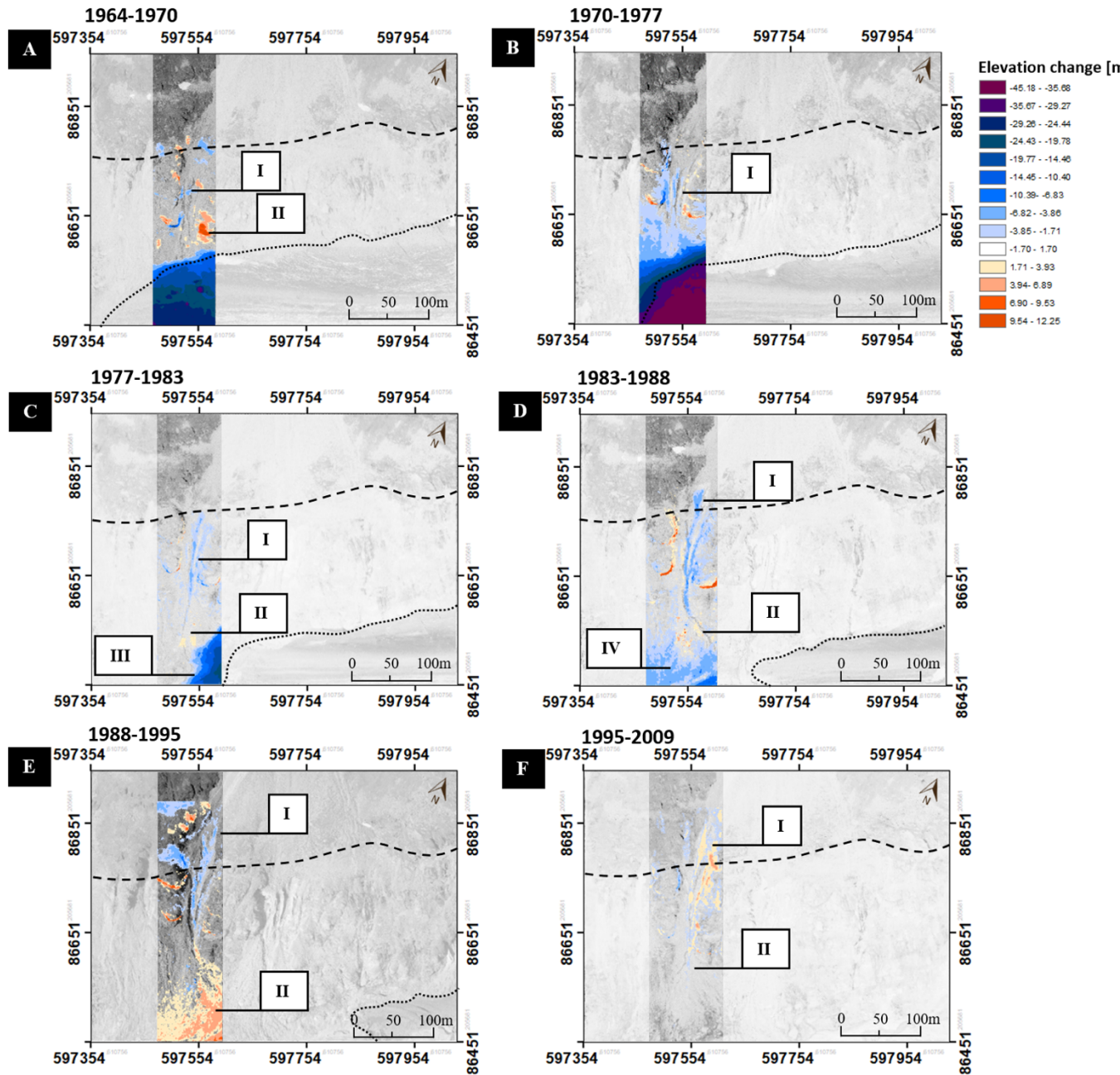


Figure 12: DEM of difference showing the historical geomorphological evolution of SS1. Dashed black line refers to the supposed LIA limit and the dotted one to the contact hillslope-glacier. Labels meaning: I = gully headward erosion, II = alluvial fan aggradation, III = valley floor exposure, IV = alluvial fan basal erosion.

1325
 1326
 1327
 1328

1329
 1330
 1331
 1332
 1333
 1334
 1335
 1336
 1337
 1338
 1339

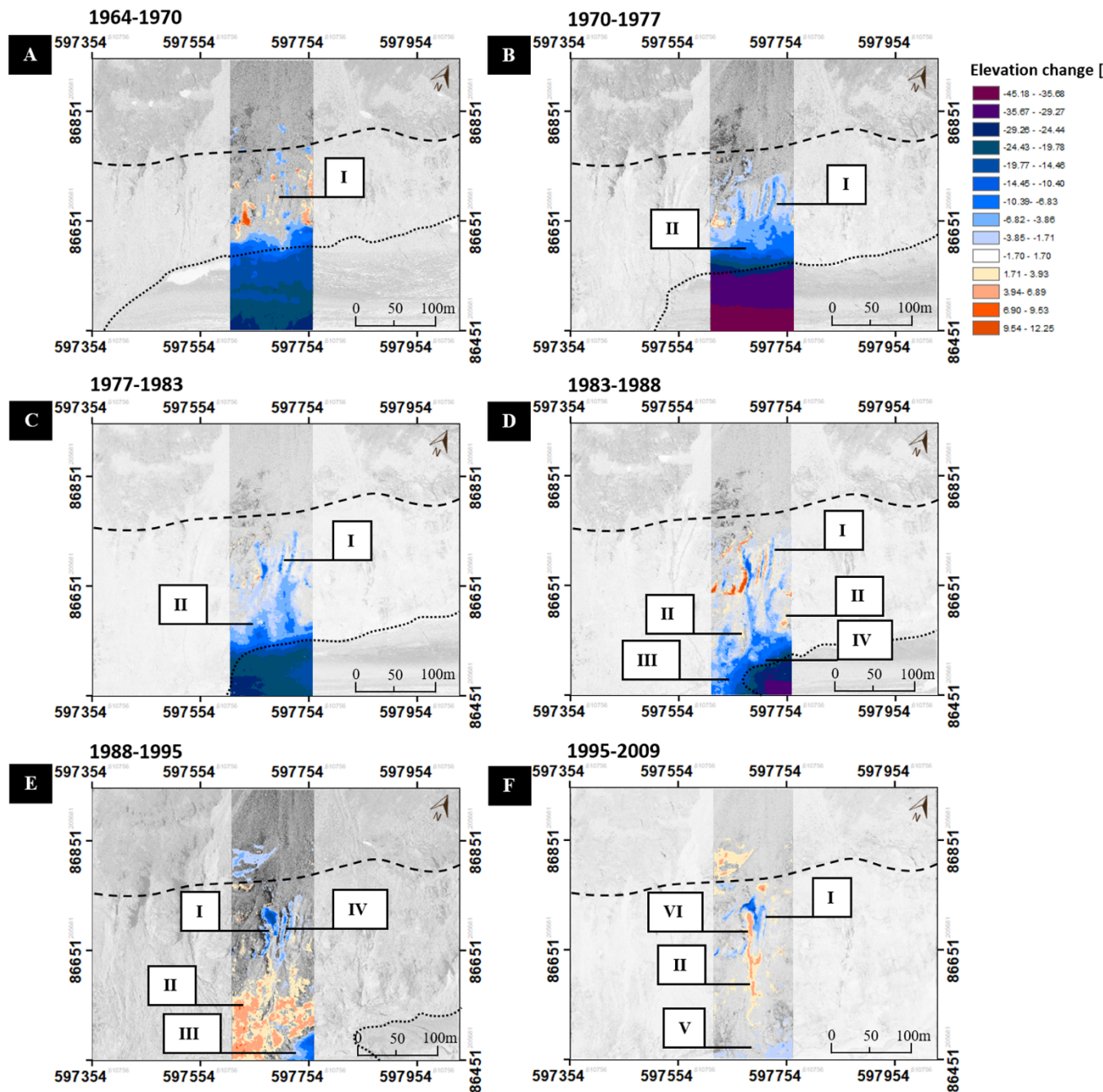


Figure 13: DEM of difference showing the historical geomorphological evolution of the SS1. Dashed black line refers to the supposed LIA limit and the dotted one to the contact hillslope-glacier. Labels meaning: I = gully headward erosion, II = alluvial fan aggradation, III = valley floor exposure, IV = bedrock patches exposure, V = alluvial fan basal erosion, VI = morainic material aggradation.

1340
1341
1342
1343

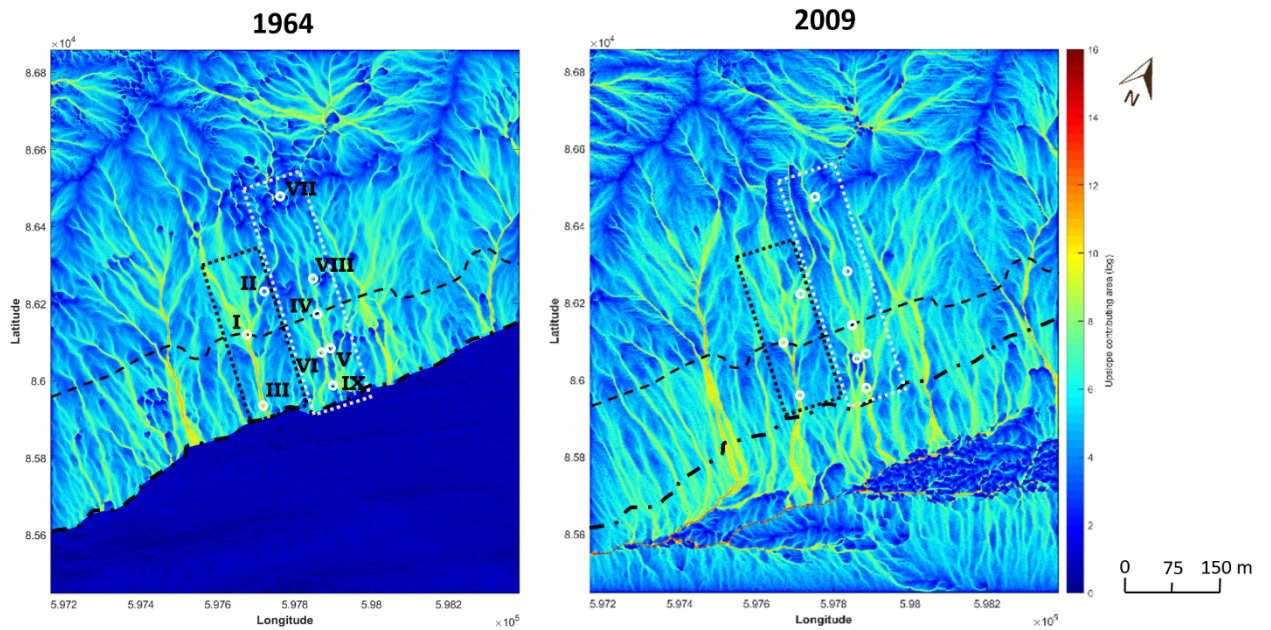
1344
1345
1346
1347
1348
1349
1350

1351



1352
1353
1354

Figure 14: Quantification of total volume of remobilized sediment per period of investigation in both subsystems (values within the LoD have not been considered).



1355
1356
1357
1358
1359
1360

Figure 15: Upslope contributing area (Flowacc algorithm) for both 1964 and 2009 DEM with all pits filled. In the 1964 DEM, the glacier surface has been masked, and is not taken into account in computation as hydrological tools require impermeable ground (Carrivick et al., 2019). Numbers and circles refer to the potential buffers in figure 17; dotted lines define SS1 (black) and SS2 (gray) limits, dashed black line represent the supposed LIA limit and the dashed-dotted black line to the contact glacier-moraine. Hillslope extent is ca. 1.1 km².

1361
1362
1363
1364
1365
1366
1367

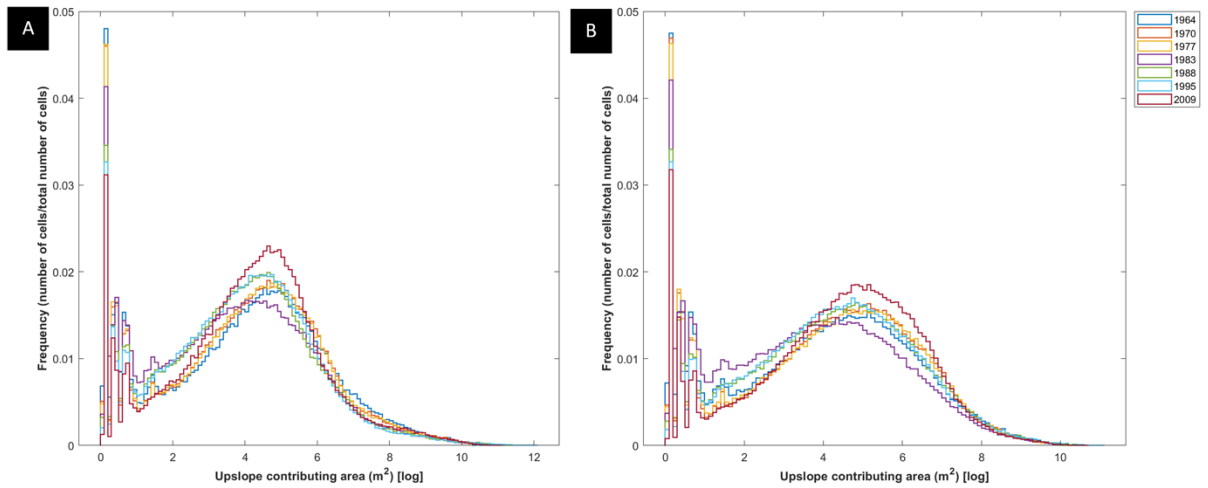


Figure 16: Histogram of flow accumulation area value for SS1 (A) and SS2 (B) in every year. Y-axis has been divided by the total number of pixels (246750 cells for SS1; 290745 cells for SS2).

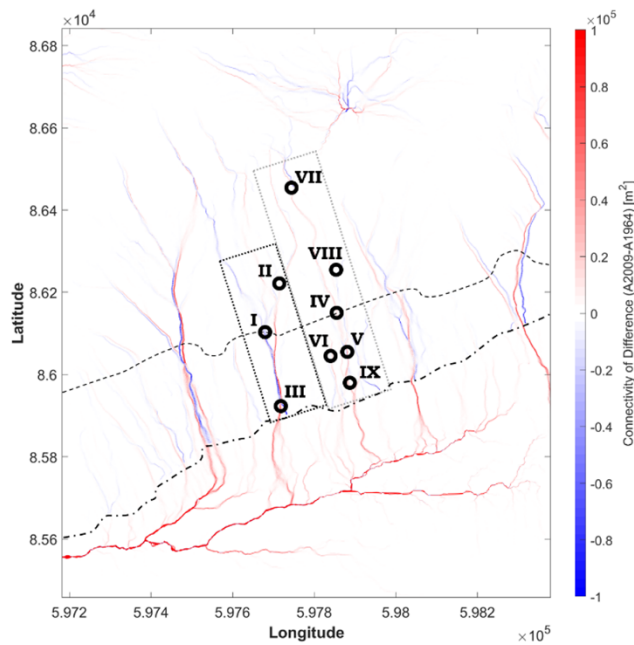


Figure 17: Changes in connectivity between 1964 and 2009. Supra-glacial streams have been masked, and are not taken into account in computation as the hydrological analyses require impermeable ground (Carrivick et al., 2019). Dotted lines define SS1 (black) and SS2 (gray) limits, dashed black line represents the supposed LIA limit and the dash-dotted black line to the contact glacier-moraine in 1964.

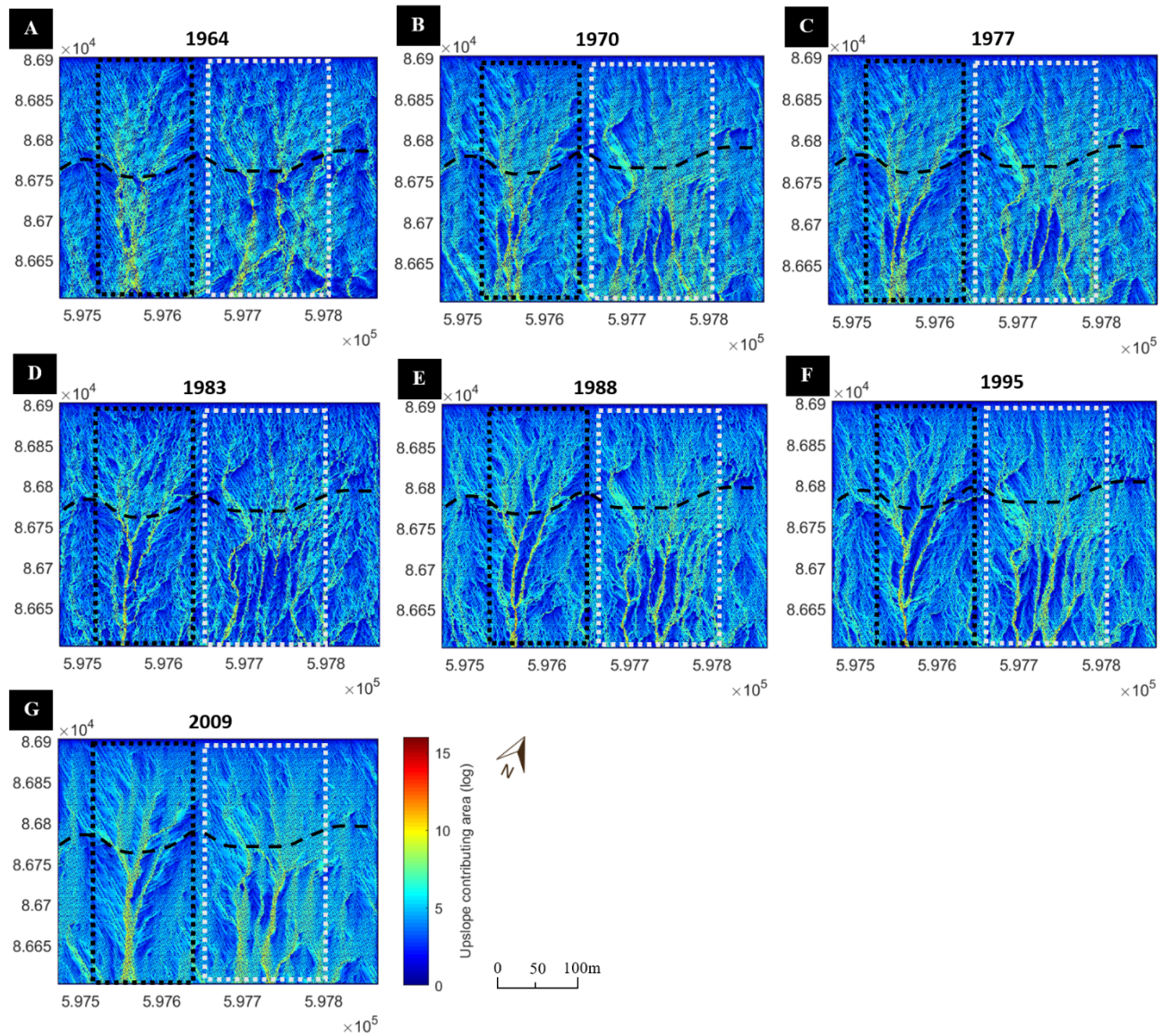


Figure 18: Evolution of upslope contributing area over time (histogram of cell values are represented in Figure 15). Dotted squares refers to SS1 and SS2 while dashed line highlight the location of the supposed LIA limit.

1386
1387
1388

1389
1390
1391
1392
1393
1394
1395
1396
1397
1398
1399
1400
1401
1402
1403

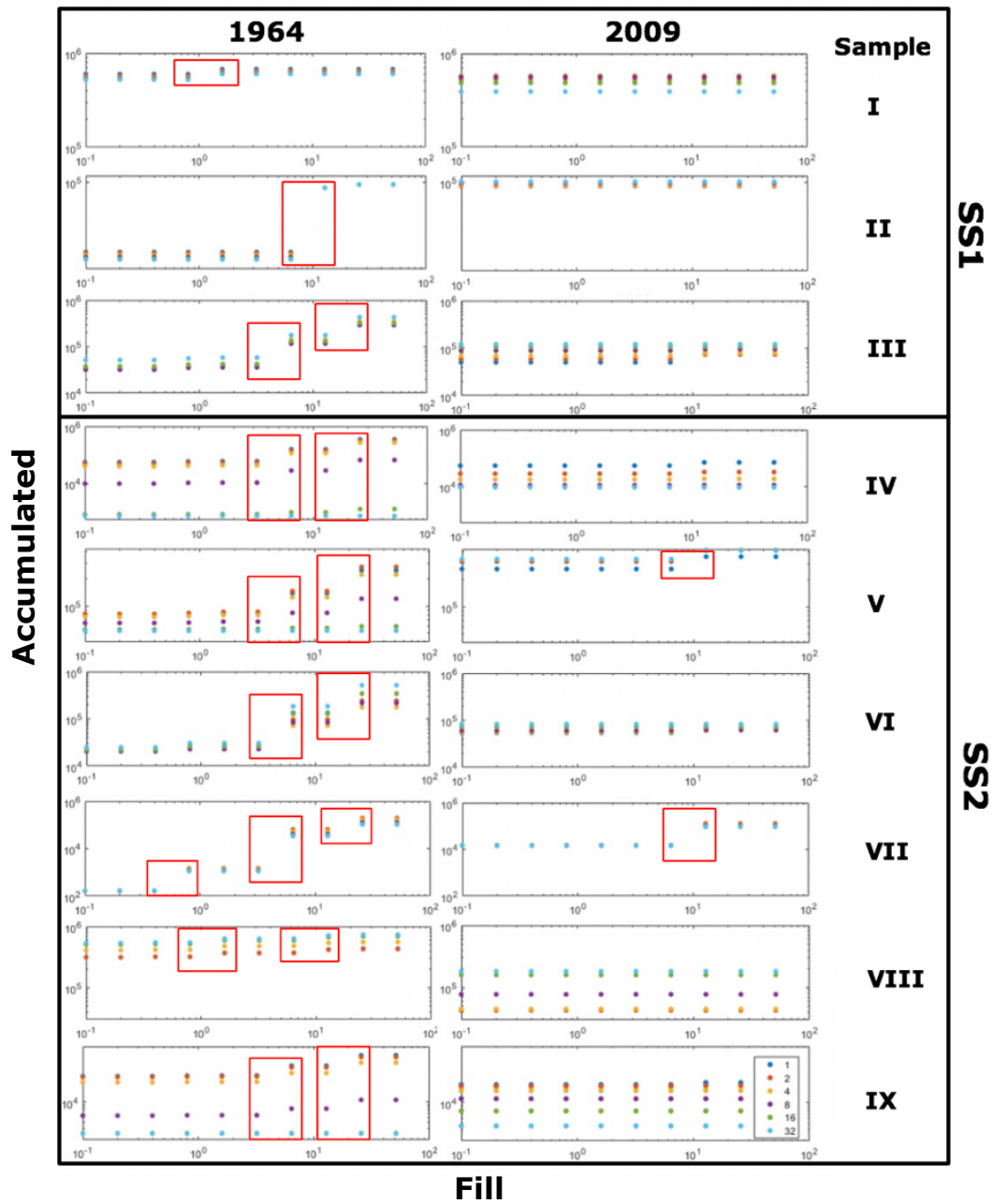


Figure 19 : Hydrological sediment connectivity quantification for 1964 and 2009 for selected regions highlighted in Figure 14. Point colors refer to the Holmgren flow routing parameters and the red squares to the increases in upslope contributing area.

1404
 1405
 1406
 1407